Modeling of the HERMES Transition Radiation Detector

by

Joseph V. Emerson

B.Sc., McGill University, 1993

A THESIS SUBMITTED IN PARTIAL FULFILLMENT
OF THE REQUIREMENTS FOR THE DEGREE OF
MASTER OF SCIENCE
in the Department
of
Physics

SIMON FRASER UNIVERSITY
July 1995

ISBN 0-612-06642-8

Canada

APPROVAL

Name: Joseph V. Emerson

Degree: Master of Science

Title of thesis: Modeling of the HERMES Transition Radiation Detector

Examining Committee: Dr. Byron Jennings
Chair

Dr. Michel Vetterli
Senior Supervisor

Prof. Otto Häusser
Dept. of Physics, S.F.U.

Prof. Howard Trottier
Dept. of Physics, S.F.U.

Dr. Doug Bryman
External Examiner
Senior Research Scientist, TRIUMF

Date Approved: July 28, 1995

PARTIAL COPYRIGHT LICENSE

I hereby grant to Simon Fraser University the right to lend my thesis, project or extended essay (the title of which is shown below) to users of the Simon Fraser University Library, and to make partial or single copies only for such users or in response to a request from the library of any other university, or other educational institution, on its own behalf or for one of its users. I further agree that permission for multiple copying of this work for scholarly purposes may be granted by me or the Dean of Graduate Studies. It is understood that copying or publication of this work for financial gain shall not be allowed without my written permission.

Title of Thesis/Project/Extended Essay

Modeling of the HERMES Transition Radiation Detector.

Author:
(signature)

Joseph V Emerson
(name)

Aug. 15th, 1995
(date)

Abstract

The HERMES transition radiation detector (TRD) is an essential component of the particle identification system in the HERMES experiment which studies the spin structure of the proton and neutron. Monte Carlo simulation of the TRD response is compared to experimental prototype data and found to be in good agreement. The simulation results are then applied in particle identification algorithms for interpretation of the HERMES TRD data.

Dedication

For my family,
in *lieu* of letters.

Acknowledgements

Foremost I would like to thank my supervisor, Mike Vetterli, for the guidance and financial support he has provided, as well as for ensuring that the past two years of hard work were also an enjoyable learning experience.

I am grateful to all members of the TRD group, and in particular Anne Trudel, Robert Henderson, and Otto Hausser, for the various ways in which they contributed to my understanding of the TRD and the HERMES experiment through the successive phases of the project.

I am also indebted to Pat Welch, Peter Green, Wolfgang Wander, Bruce Bray, Machiel Kolstein, and many other members of the HERMES collaboration for their assistance and contributions.

Finally, I would like to thank Andy Miller for the many invaluable criticisms and insights to which I owe much of the success of the present work.

Contents

Abstract iii
Dedication iv
Acknowledgements v
List of Tables viii
List of Figures ix
1 Introduction 1
2 The HERMES Experiment 4
2.1 Deep Inelastic Scattering Theory 4
2.2 Proposed Measurements 9
2.3 Description of the Experiment 14
3 The HERMES Transition Radiation Detector 20
3.1 Transition Radiation Theory 20
3.2 TRD Design Principles 23
3.3 The HERMES TRD Physical Design 28
3.3.1 The Radiator 29
3.3.2 The X-ray Detector 29
3.3.3 The Gas System and Flush Gaps 31
4 TRD Prototype Tests 32
4.1 Overview of Test Experiment 33
4.2 Method of Analysis 33
4.3 Results of Analysis 37
4.3.1 The Fibre Radiators 37
4.3.2 The Foil Radiator 39

4.3.3 The Foam Radiators 39
4.3.4 Summary of Results 39
5 Monte Carlo Simulation of the TRD 45
5.1 Overview and Motivation 46
5.2 Theory of Energy Loss 47
5.2.1 Ionisation Energy Loss 48
5.2.2 Absorption of X-ray Radiation 49
5.3 Description of the Monte Carlo Simulation 50
5.3.1 Modeling of Ionisation Energy Loss 52
5.3.2 Modeling of Transition Radiation 59
5.3.3 Modeling of Photoabsorption 61
5.4 Comparison to Experimental Data 61
5.5 Study of HERMES TRD Response Distributions 62
5.5.1 Momentum Dependence of Response Distributions . 66
5.5.2 Angular Dependence of Response Distributions . . . 66
5.5.3 Simulation Results for Detector Effects 68
5.5.4 Monte Carlo Generation of Response Distributions . 71
6 Particle Identification Analysis 75
6.1 Overview of Probability Method 75
6.2 Maximum Likelihood and Bayes Theorem 79
6.3 Particle Identification Algorithms 80
6.3.1 TRD PID Algorithm 81
6.3.2 Proposed HERMES PID Algorithm 82
7 Conclusion 84
Appendix: Contribution to HERMES 86
Bibliography 88

List of Tables

2.1 Experimental Results and Theoretical Predictions for Sum Rules . . . 13

4.1 PRFs for the Different Radiator Types 44

List of Figures

1.1 Schematic of Lepton-Nucleon Scattering 2

2.1 Feynman Diagram 6
2.2 HERMES Spectrometer 15
2.3 The Kinematic Plane 16

3.1 Typical Response Distributions in Total Energy Deposition Method . 26
3.2 Impact of Transition Radiation on Electron Distribution 27
3.3 Cross section of TRD Module 28

4.1 Impact of Truncated Mean Method 35
4.2 17–20 μ Fibre Radiator 38
4.3 25–30 μ Fibre Radiator 40
4.4 Quasi-Ideal 15.2 μ Foil Radiator 41
4.5 R-Foam Radiator 42
4.6 H-Foam Radiator 43

5.1 Comparison of PAI Model to Data with 5 keV Cuts 55
5.2 Comparison of PAI Model to Data with 10 keV Cuts 56
5.3 Comparison of Urban Model to Data with 5 keV Cuts 57
5.4 Comparison of Urban Model to Data with 10 keV Cuts 58
5.5 Simulation Comparison to Data at 5 GeV 63
5.6 Simulation Comparison to Data at 10 GeV 64
5.7 Momentum Dependence of Response Distributions 67
5.8 Angular Dependence of Response Distributions 69

5.9 Module Dependence of Response Distributions 70
5.10 Wire Sum Dependence of Response Distributions 72
5.11 Effect of Wire Sum on Truncated Mean 73

6.1 Response Distributions Scaled by Flux Ratio 77
6.2 Truncated Mean Spectra Scaled by Flux Ratio 78

Chapter 1

Introduction

The HERMES experiment has been designed to study the internal spin structure of the nucleon. The precise spin structure of the nucleon has become a subject of much theoretical and experimental interest since the measurement of the European Muon Collaboration (EMC) experiment which indicated that the net spin of the quarks constitutes only a small fraction of the nucleon spin [1]. This unexpected result, which begat the nucleon 'spin-crisis', has since been confirmed by other experiments at CERN (European Center for Nuclear Research) and SLAC (Stanford Linear Accelerator). This agreement with the unexpected EMC result reveals that the actual origin of the nucleon spin remains an open question. In particular, the relative contributions of valence quarks, sea quarks, gluons, and orbital angular momentum, if any, must be measured to determine the origin of the nucleon spin.

In the HERMES deep inelastic scattering experiment 27.5 GeV polarised positrons from the HERA storage ring are used as probes of the internal structure of polarised nucleon targets. Through measurement of the distributions in energy and angle of the scattered positron, information can be deduced about the nature of the interaction between the incident positron and the internal nucleon constituents; in particular, the dependence of these distributions on the relative polarisation of the positron-nucleon system is a measure of the polarisation of the quarks inside the nucleon. A schematic of the experiment is given in fig. 1.1 where only the detection of the final state positron is shown. In general, however, measurement of coincident final

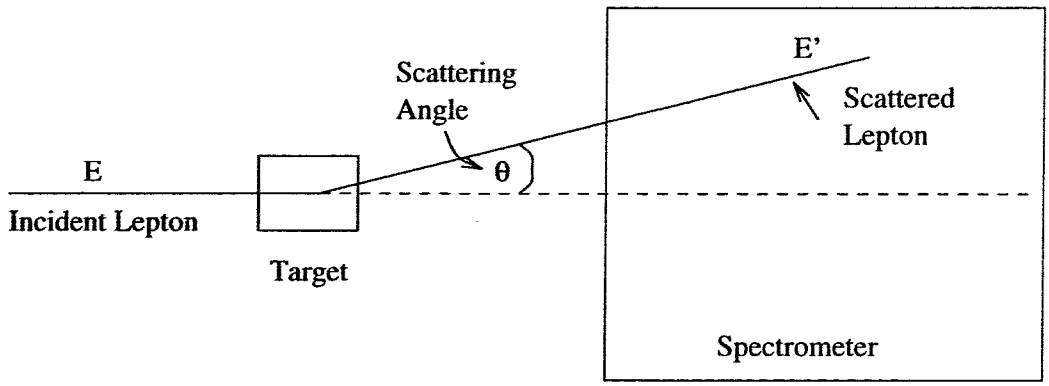

Figure 1.1: Schematic of lepton-nucleon scattering in the lab frame.

state nucleon fragments is a unique strength of the HERMES spectrometer and such measurements will provide first insight into the flavour dependent polarisation of the valence and sea quarks. Measurement of a significant sea quark contribution to the nucleon spin could explain the existing disagreement between current experimental results and theoretical prediction [2]. An introduction to the theory of polarised deep inelastic scattering, an overview of the proposed measurements, and a description of the HERMES spectrometer will be presented in chapter 2.

Efficient determination of the identity of the measured final state particles is critical for the HERMES experiment to reach its physics goals. Particle identification (PID) is needed not only for discrimination of the DIS positron against any hadrons coincident with the DIS event, but, more importantly, for discrimination of DIS positrons against the more significant hadronic background from non-DIS photoproduction events.

One essential component of the PID instrumentation in the HERMES spectrometer is a transition radiation detector (TRD) developed by the Canadian HERMES group at TRIUMF. This relatively new detector type provides ultrarelativistic particle identification based on the Lorentz factor γ of the incident particle. This sensitivity to γ, rather than the velocity β, allows for greater identification power over conventional velocity dependent PID detectors in the comparatively compact space available in the HERMES spectrometer. The sensitivity to the Lorentz factor results from the explicit generation and subsequent detection of γ dependent transition radiation in

the TRD. The theory of transition radiation, general TRD design principles, and the specific design of the HERMES TRD are the subject of chapter 3.

The design of the HERMES TRD was guided by prototype tests and computer, or Monte Carlo, simulation. The prototype tests were performed at CERN and focused on the comparison of different radiator materials for the TR generation. These prototype tests served as a confirmation of the adequate performance of the preferred radiator material and also provided an important standard of comparison for simulation. Monte Carlo simulation was then used to optimise the final HERMES TRD design. The analysis of these prototype test results is described in chapter 4.

Monte Carlo simulation of detector performance has become an important tool in high energy physics. In addition to its usefulness in optimisation of detector design, simulation has also become an essential tool in the analysis of experimental results. A Monte Carlo simulation (HMC) of the complete HERMES spectrometer was developed to address these needs. For compatibility with the detector simulation tool chosen as the basis for the HMC, namely GEANT, a Monte Carlo simulation of the HERMES TRD was developed and compared to the prototype TRD data to test and optimise the GEANT algorithms in the modeling of the critical low energy physics processes to which the TRD performance is uniquely sensitive. The description and optimisation of the GEANT based TRD simulation will be presented in chapter 5.

One important application of the TRD simulation results is in the interpretation of the TRD data. Predetermined TRD response distributions are required by the PID algorithms which convert the energy deposition in the TRD detectors into a probabilistic determination of the incident particle type. The application of the TRD Monte Carlo simulation to the determination of these response distributions is also presented in chapter 5 and the PID algorithms developed for interpreting the TRD data are the subject of chapter 6.

Chapter 2

The HERMES Experiment

The HERMES experiment has been developed to study the spin structure of the proton and neutron through measurements of the deep inelastic scattering of polarised leptons (either electrons or positrons) from polarised nucleons. This chapter first reviews the theory of deep inelastic lepton scattering and discusses its interpretation in terms of internal nucleon structure. The proposed measurements are then introduced along with a discussion of the theoretical predictions for these quantities. In the final section the physical design of the experiment is presented for completeness as well as for necessary background to the specific role of the HERMES transition radiation detector.

2.1 Deep Inelastic Scattering Theory

As an introduction to, and background for, the study of polarised deep inelastic lepton scattering , it is instructive to first review unpolarised deep inelastic scattering (DIS) theory and its implications for our understanding of nucleon structure. In particular, the results of unpolarised DIS theory and experiment will both motivate and illuminate the interpretation of the spin structure of the nucleon as revealed through *polarised* DIS experiments. The exposition below on unpolarised DIS theory follows closely that of reference [3].

The *deep* inelastic scattering of a lepton from a nucleon is distinguished from the

more general inelastic case through the assumption of quasi-elastic scattering with the nucleon's internal constituents. Without any *a priori* knowledge of this internal structure the DIS cross section can be parametrised by five unknown functions of the available combinations of the kinematic parameters, dubbed structure functions.

From constraints imposed by the theory of quantum electrodynamics, such as conservation of electromagnetic current and conservation of parity in the absence of weak interactions, these unknown structure functions can be reduced to only two *independent* functions, and the cross section takes the following conventional form in the lab frame where the nucleon is at rest,

$$\frac{d^2\sigma}{dE'd\Omega} = \frac{\alpha^2}{4E^2\sin^4\frac{\theta}{2}}\left\{ W_2(\nu,Q^2)\cos^2\frac{\theta}{2} + 2W_1(\nu,Q^2)\sin^2\frac{\theta}{2} \right\} \tag{2.1}$$

where $W_{1,2}$ are the unknown structure functions, E is the energy of the incident lepton, E' is the energy of the scattered lepton, α is the fine structure constant, θ is the scattering angle, and the Lorentz-invariant kinematic variables for the four-momentum and energy of the exchanged photon, $q^2 = -Q^2$ and ν respectively, are given in the lab frame by,

$$q^2 = -4EE'\sin^2\frac{\theta}{2} \tag{2.2}$$

$$\nu = E - E'. \tag{2.3}$$

For sufficiently high Q^2 events, the virtual photon's corresponding shorter wavelength is anticipated to resolve any internal nucleon constituents, and the scattering process may be interpreted as an interaction between the virtual photon and these nucleon constituents, called 'partons'. If these partons can be considered to be free structureless spin-1/2 particles, then the parametrised cross section, given by eq. 2.1, should reduce to the well-known cross section for the elastic scattering between two free distinguishable Dirac particles, as demonstrated schematically in fig. 2.1. This correspondence implies the identities

$$\begin{aligned} MW_1(\nu,Q^2) &\longrightarrow F_1\left(\frac{Q^2}{2M\nu}\right), \\ \nu W_2(\nu,Q^2) &\longrightarrow F_2\left(\frac{Q^2}{2M\nu}\right), \end{aligned} \tag{2.4}$$

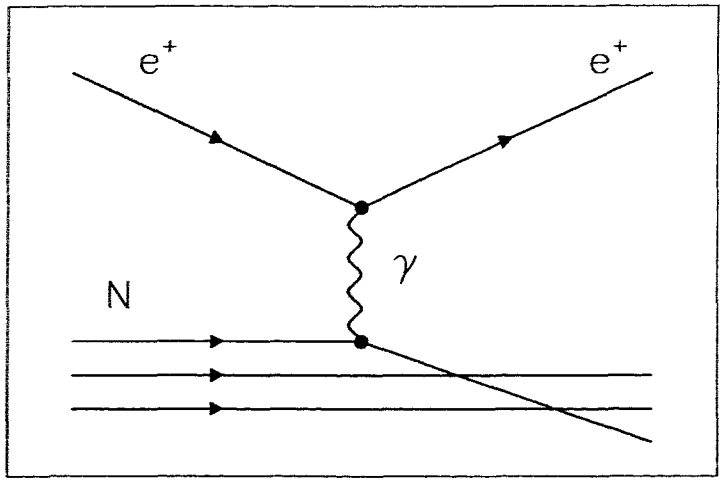

Figure 2.1: The Feynman diagram for lepton-parton scattering in the nucleon.

where M is the nucleon mass and F_1 and F_2 are new structure functions which exhibit the interesting property of becoming functions of only one variable, namely the ratio $\frac{Q^2}{2M\nu}$. Another important theoretical consequence of the simple identification of partons with free Dirac particles is the Callan-Gross relation

$$2xF_1\left(\frac{Q^2}{2M\nu}\right) = F_2\left(\frac{Q^2}{2M\nu}\right). \tag{2.5}$$

The independence of the structure functions F_1 and F_2 on Q^2 or ν separately is known as Bjorken scaling.

For a more formal treatment of the parton model of the nucleon, a momentum probability distribution $f_i(x)$ is introduced where each parton i is considered to carry a momentum fraction x of the nucleon's momentum. When the kinematics of the scattering process are considered in the infinite momentum frame, or Breit frame, where both nucleon and parton masses can be neglected, then the parton momentum fraction x can be shown to be equal to the ratio $\frac{Q^2}{2M\nu}$, and this ratio becomes the single independent scaling variable determining the structure functions.

The identity between momentum fraction x and the kinematic observable $\frac{Q^2}{2M\nu}$ allows for the interpretation of experimental results as measurements of the momentum

distributions of the various parton types in the nucleon, that is

$$F_2(x) = \sum_i e_i^2 x f_i(x), \tag{2.6}$$

where e_i is the charge of parton i. As an immediate example of the interpretation of F_2, consider a simplistic model of the nucleon consisting of n equal mass non-interacting partons. In this case one would anticipate to find the measured structure function strongly peaked, in fact resembling a delta function, at a momentum fraction $x = 1/n$.

Precise measurements of the unpolarised structure functions have been used to test whether the partons of the above model may indeed be identified with the quarks (and gluons) of Quantum Chromodynamics (QCD). Within this more sophisticated framework, known as the Quark Parton Model (QPM), consideration of gluon exchange between the 3 constituent quarks predicts a smearing of the quark momentum distribution about the peak value at $x = 1/3$. Further, as a result of the virtual production of quark anti-quark pairs by the gluons in the nucleon, an increase in the distribution of quarks at low x values, that is, at low momentum fractions, is also expected.

The above effects, and the QPM, have been well established by the data: the parton constituents can be consistently identified with the spin-1/2 quarks anticipated from hadron spectroscopy. Further, analysis of the momentum distributions of the quarks inside the nucleon leads to the conclusion that a substantial fraction of the nucleon momentum is unaccounted for by the quarks and is in fact carried by the massless gluons.

Before proceeding to the study of the nucleon spin structure, it is important to point out that both the Callan-Gross relation and Bjorken scaling are based on the simple identification of the partons with free Dirac particles and are therefore only first order approximations. The small deviations that have been experimentally observed are known as scaling violations and arise due to QCD correction factors such as internal gluon Bremsstrahlung. These deviations show F_2 increasing with Q^2 for $x < 0.25$ and decreasing with Q^2 for $x > 0.25$, corresponding to large momentum fraction quarks appearing as low momentum fraction quarks due to gluon emission.

The size of these deviations can be as large as 50% at the low x and high x extremes, over an order of magnitude range in Q^2.

Thus the structure functions must be generalised to include dependence on two variables, conventionally chosen as x and Q^2, and the deviations from the Callan-Gross relation are reflected in the function $R(x, Q^2)$ where

$$F_1(x, Q^2) = \frac{F_2(x, Q^2)}{2x[R(x, Q^2) + 1]} \left[1 + \frac{Q^2}{\nu^2}\right]. \tag{2.7}$$

In the case of *polarised* DIS the concepts above are extended to the analysis of the spin content of the nucleon, where differences in the cross section for various relative orientations of spin direction between the incident lepton beam and the nucleon target are measured. Two spin structure functions, G_1 and G_2, are introduced to represent the nucleon spin structure and the differences in the cross sections can be written [4],

$$\frac{d^2\sigma^{\uparrow\downarrow}}{dQ^2 d\nu} - \frac{d^2\sigma^{\uparrow\uparrow}}{dQ^2 d\nu} = \frac{4\pi\alpha^2}{Q^2 E^2}\left\{M(E + E'\cos\theta)G_1(Q^2, \nu) - Q^2 G_2(Q^2, \nu)\right\}, \tag{2.8}$$

and,

$$\frac{d^2\sigma^{\uparrow\rightarrow}}{dQ^2 d\nu} - \frac{d^2\sigma^{\uparrow\leftarrow}}{dQ^2 d\nu} = \frac{4\pi\alpha^2 E'}{Q^2 E^2}\sin\theta\left\{MG_1(Q^2, \nu) + 2EG_2(Q^2, \nu)\right\}. \tag{2.9}$$

where the arrows denote relative polarisation of the beam and target respectively. Thus eq. 2.8 represents scattering with the polarisation of both the beam and target along the beam direction and eq. 2.9 represents scattering with beam polarisation parallel to the beam direction and target polarisation transverse to the beam direction. These *two* measurements of the differences in the cross sections allow for complete determination of the two independent spin structure functions G_1 and G_2.

For high Q^2 events scaling is anticipated and the identities

$$M^2\nu G_1(Q^2, \nu) \longrightarrow g_1(x) \tag{2.10}$$

$$M\nu^2 G_2(Q^2, \nu) \longrightarrow g_2(x) \tag{2.11}$$

emerge. Due to the scaling violations mentioned previously, modern high precision experiments require the generalisation of $g_1(x)$ and $g_2(x)$ to $g_1(x, Q^2)$ and $g_2(x, Q^2)$.

In analogy to the interpretation of F_2 in terms of constituent momentum distributions in the Breit frame, g_1 can be written

$$g_1(x) = \sum_f e_f^2[q_f^+(x) - q_f^-(x)], \tag{2.12}$$

where $q^{+(-)}$ is the distribution of quarks with spin parallel (anti-parallel) to the nucleon spin and the sum is over quark flavours [5].

However, experimental measurements indicate that the spin of the quarks constitute at most 50% of the nucleon spin. Thus, in general, the spin of the nucleon is expressed as,

$$\langle S_z \rangle = \frac{1}{2}(\Delta V + \Delta S) + \Delta G + L_z, \tag{2.13}$$

where ΔV denotes the valence quark contribution, ΔS the sea quark contribution, ΔG the net spin of the gluons, and L_z any orbital angular momentum contribution to the nucleon spin [5]. Semi-inclusive measurements are required for identification of the individual contributions of each term in eq. 2.13 to the nucleon spin.

2.2 Proposed Measurements

The HERMES experiment will measure the asymmetries $A_{\parallel}$ and $A_{\perp}$ which denote scattering with longitudinal and transverse target polarisation respectively. The asymmetries are given by,

$$A_{\parallel} = \frac{\sigma^{\uparrow\uparrow} - \sigma^{\uparrow\downarrow}}{\sigma^{\uparrow\uparrow} + \sigma^{\uparrow\downarrow}}, \tag{2.14}$$

$$A_{\perp} = \frac{\sigma_{\perp}^{\uparrow\uparrow} - \sigma_{\perp}^{\uparrow\downarrow}}{\sigma_{\perp}^{\uparrow\uparrow} + \sigma_{\perp}^{\uparrow\downarrow}}, \tag{2.15}$$

where $\sigma^{\uparrow\uparrow} - \sigma^{\uparrow\downarrow}$ is shorthand for the difference in the cross sections with the two different longitudinal target-spin orientations, as given by eq. 2.8, and $\sigma_{\perp}^{\uparrow\uparrow} - \sigma_{\perp}^{\uparrow\downarrow}$ is shorthand for the difference in the cross sections with the two different transverse target polarisations, as given by eq. 2.9. The sum in the denominator is a conventional normalisation factor.

The measurement with transverse relative polarisation is not azymuthally symmetric and $\sigma_\perp$ is determined by

$$\sigma_\perp = \int \frac{1}{\cos\phi}\frac{d\sigma}{d\phi}d\phi, \tag{2.16}$$

where ϕ is the angle between the polarisation plane and the scattering plane.

Note that the above asymmetries assume 100% target and beam polarisation. In practice these asymmetries are extracted from a measured asymmetry,

$$A_{meas} = A_{\parallel} \cdot P_t \cdot P_b \cdot f. \tag{2.17}$$

Here $P_{t(b)}$ is the target(beam) polarisation and f is the fraction of polarisable nucleons in the target.

The experimental asymmetries $A_{\parallel}$ and $A_\perp$ relate to the virtual photon asymmetries A_1 and A_2 which directly reflect the photon-nucleon absorption cross sections, defined by

$$A_1 = \frac{\sigma_{1/2} - \sigma_{3/2}}{\sigma_{1/2} + \sigma_{3/2}}, \tag{2.18}$$

$$A_2 = \frac{\sigma_{TL}}{\sigma_T}, \tag{2.19}$$

where the subscripts 1/2 and 3/2 refer to the projection of the total angular momentum of the photon-nucleon system along the incident lepton direction, σ_T is the total transverse photon-nucleon cross section, and σ_{TL} is an interference term between the transverse and longitudinal amplitudes.

The relationship between the lepton-nucleon and photon-nucleon asymmetries is given by

$$A_{\parallel} = D \cdot (A_1 + \eta \cdot A_2) \tag{2.20}$$

$$A_\perp = d \cdot (A_2 - \xi \cdot A_1), \tag{2.21}$$

where

$$D = \frac{y(2-y)}{y^2 + 2(1-y)(1+R)} \tag{2.22}$$

$$\eta = \frac{2\gamma(1-y)}{(2-y)} \tag{2.23}$$

$$d = D\sqrt{\frac{2\epsilon}{1+\epsilon}} \tag{2.24}$$

$$\xi = \eta\frac{1+\epsilon}{2\epsilon}. \tag{2.25}$$

Here $R = \sigma_L/\sigma_T$ is the ratio of longitudinal to transverse virtual photoabsorption cross sections and $y = \nu/E$ is a standard kinematic variable which equals the fraction of the incident lepton energy transferred in the scattering process. The factors D and d arise from depolarisation of the virtual photon and ϵ reflects the degree of transverse polarisation of the virtual photon [6]. The fact that the kinematic factors η and ξ are small reveals that there is a strong correlation between A_1 and $A_{||}$ and between A_2 and $A_\perp$.

Within the framework of the QPM, A_1 and A_2 are related to g_1 and g_2 as follows,

$$A_1 = \frac{g_1 - \gamma^2 g_2}{F_1} \tag{2.26}$$

$$A_2 = \frac{\gamma(g_1 + g_2)}{F_1} \tag{2.27}$$

where $\gamma = \frac{\sqrt{Q^2}}{\nu}$ and F_1 is the spin-independent structure function.

The determination of the experimental asymmetries, and thus the spin structure functions, over the range $0.02 < x < 0.8$, coupled with a theoretical model for the extrapolations $x \to 0$ and $x \to 1$, also allows for an experimental test of the theoretical sum rules which predict the values of the integrals of g_1 and g_2 for the proton and neutron over the full x range.

Foremost in significance is the fundamental Bjorken sum rule,

$$\int_0^1 [g_1^p(x) - g_1^n(x)]dx = \frac{1}{6}\frac{g_A}{g_V}(1 - \frac{\alpha_s}{\pi} + \mathcal{O}(\alpha_s^2)), \tag{2.28}$$

including first order QCD corrections [7]. Eq. 2.28 requires only light cone current algebra and QCD to predict the integral over x of the difference of the proton and neutron structure functions in terms of the well-known coupling constants g_A and g_V from neutron beta decay and α_s from QCD . The Bjorken sum rule thus amounts essentially to a test of QCD itself.

Ellis and Jaffe derived sum rules for the proton and neutron separately,

$$\int_0^1 g_1^{p(n)}(x)dx = \frac{1}{12}\frac{g_A}{g_V}\left(+(-)1 + \frac{5}{3}\frac{3F/D-1}{F/D+1}\right) \times QCD\ corrections, \qquad (2.29)$$

assuming exact SU(3) flavour symmetry and that the strange sea has no net polarisation, *ie.* $\Delta s = 0$ [2]. F and D are SU(3) couplings determined from a fit to available neutron and hyperon β decay data. The value of the Ellis-Jaffe sum rule is very sensitive to changes in the experimental fit of the ratio F/D as well as QCD correction factors. Subject to this caveat, violation of this sum rule is evidence that $\Delta s \neq 0$ [8].

As mentioned in the introduction, the EMC experiment at CERN, through polarised muon scattering from polarised proton targets, first measured the surprising result for g_1^p that violated the Ellis-Jaffe sum rule and thus initiated the nucleon 'spin crisis' [1, 9]. Other experiments were then developed both to check the EMC results as well as to explore the spin content of the neutron.

The SMC (Spin Muon Collaboration) experiment, also at CERN, scattered polarised muons from both polarised deuteron and proton targets to measure g_1^d [10] and g_1^p [11] respectively. In parallel, experiments E142 and E143 at SLAC, which scattered polarised electrons from polarised ^{3}He, proton, and deuteron targets, produced results for g_1^n [12], g_1^p [13], and g_1^d [14]. The experimental results for the Ellis-Jaffe and Bjorken sum rules from EMC , SMC, and SLAC are summarised in table 2.1 [15]. The theoretical predictions for these results as well as the anticipated uncertainty from HERMES [6] are also presented in table 2.1 for comparison.

Another important sum rule has been derived by Burkhardt and Cottingham for the integral of g_2,

$$\int_0^1 dx g_2(x, Q^2) = 0, \qquad (2.30)$$

which results from angular momentum conservation, or, equivalently, rotational symmetry [17]. HERMES anticipates to measure this sum rule with a statistical uncertainty of $\pm.017$ [6].

HERMES will also provide first measurements of the spin-dependent structure functions $b_1(x)$ and $\Delta(x)$ associated with nuclear binding effects in the spin-1 deuteron target [6]. These structure functions are measured with the beam unpolarised but with

Table 2.1: Experiment results and theoretical predictions for sum rules compared to HERMES anticipated uncertainty, combined systematic and statistical errors.

Ellis-Jaffe (proton):

experiment (target)	result	theory	$\langle Q^2 \rangle$
EMC (NH_3)	$0.126 \pm .010 \pm .015$	$0.189 \pm .005$	10 GeV^2
SMC (C_4H_9OH)	$0.136 \pm .011 \pm .011$	$0.176 \pm .006$	10 GeV^2
E143 (NH_3)	$0.127 \pm .004 \pm .01$	$0.160 \pm .006$	3 GeV^2
HERMES (H)	$\pm .007$	–	–

Ellis-Jaffe (neutron):

experiment (target)	result	theory	$\langle Q^2 \rangle$
SMC (C_4D_9OD) & EMC (NH_3)	$-0.08 \pm .04 \pm .04$	$0.002 \pm .005$	4.6 GeV^2
E142 (^3He)	$-0.022 \pm .007 \pm .009$	$-0.021 \pm .018$	2 GeV^2
HERMES (^3He)	$\pm .007$	–	–
HERMES (D & H)	$\pm .009$	–	–

Bjørken:

experiment (targets)	result	theory	$\langle Q^2 \rangle$
SMC (C_4D_9OD) & EMC (NH_3)	$0.20 \pm .05 \pm .04$	$0.191 \pm .002$	4.6 GeV^2
SMC (C_4H_9OH) & SMC (C_4D_9OD) & E142 (^3He)	$0.163 \pm .017$	$0.185 \pm .004$	5 GeV^2
E142 (^3He) & EMC (NH_3)	$0.146 \pm .021$	$0.183 \pm .007$	2 GeV^2
E143 (NH_3) & E142 (^3He)	$0.149 \pm .014$	$0.171 \pm .008$	3 GeV^2
HERMES (H & ^3He)	$\pm .010$	–	–
HERMES (H & D)	$\pm .015$	–	–

the target polarised parallel (for b_1) or perpendicular (for Δ) to the incident beam direction.

The interesting possibility of polarisation of the quark sea is suggested by experimental disagreement with the Ellis-Jaffe sum rule prediction. Because of the open acceptance of the spectrometer, the HERMES experiment is in the unique position to *directly* determine the existence of any sea polarisation contribution to the nucleon spin through semi-inclusive measurements of hadrons coincident with the DIS event. Semi-inclusive refers to a measurement of the type

$$\vec{e} + \vec{N} \rightarrow e' + h + X \tag{2.31}$$

where the arrows are a reminder of polarisation, h denotes the measured final state

hadron, and X represents the remaining unmeasured nucleon fragments.

The final state hadron can be identified with the struck quark if it satisfies certain kinematic criteria, as shown by Berger [16], depending on the rapidity y_h and energy fraction z_h of the leading hadron. The rapidity of the hadron is given by

$$y_h = \frac{1}{2} ln \left[\frac{E_h + p_{h,L}}{E_h - p_{h,L}} \right], \tag{2.32}$$

where $p_{h,L}$ denotes the longitudinal component of the hadron momentum along the direction of the virtual photon's momentum, and z_h can be approximated by E_h/E_γ. This semi-inclusive tag on the spin asymmetries allows for the first experimental measurement by HERMES of the important *flavour* dependence in the quark helicity distributions, that is, the relative contribution to $g_1(x)$ from each term in eq. 2.12, and is thus sensitive to sea quark $(\bar{u}, \bar{d}, s, \bar{s})$ contributions to the nucleon spin.

Finally, the open acceptance of the spectrometer offers the further advantage of unpolarised measurements of the pion charge asymmetry. This information will help elucidate the correct model explaining experimental deviation from the Gottfried sum rule which predicts the quark charges.

2.3 Description of the Experiment

The longitudinally polarised positrons in the HERA storage ring are scattered from internal gas targets into the HERMES magnetic spectrometer. For determination of the proton structure functions a hydrogen gas target is used and for the determination of the neutron structure functions two different gases, ^{3}He and deuterium, are used. These two independent measurements compensate for the fact that the neutron targets are necessarily nuclear, and therefore inevitably contaminated with protons. In the case of ^{3}He the spin of the protons cancel to good approximation and thus spin dependent asymmetries can be ascribed to the neutron. The neutron structure functions are determined from the deuterium target by simply subtracting out the independently measured proton contribution.

The gas targets offer the advantages of rapid reversal of spin direction to minimise systematic error as well as superior purity over conventional solid targets. For a

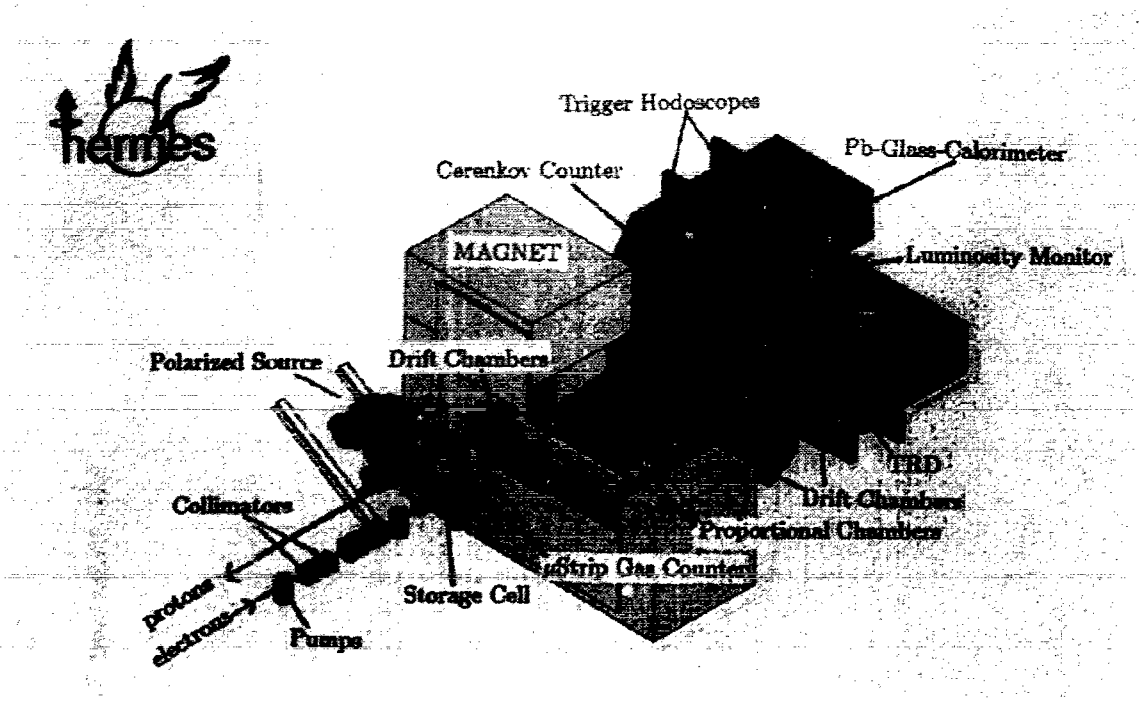

Figure 2.2: The HERMES spectrometer.

conventional solid target, such as ammonia (NH_3), the dilution factor, f from eq. 2.17, is of order 3/17. On the other hand the HERMES targets are essentially pure atomic species, with f equal to 1 for H and D. The effect of f on the statistical uncertainty of the asymmetries is significant since

$$\delta A_{\parallel} = \frac{1}{\sqrt{N^{\uparrow} + N^{\downarrow}}} \frac{1}{p_T p_B f}. \tag{2.33}$$

The net running time for pure targets is thus reduced by a factor f^2 over the case for the impure solid targets.

The open acceptance of the HERMES magnetic spectrometer allows for measurement of the scattered positron as well as any coincident hadrons. A schematic view of the spectrometer is given in fig. 2.2, from which it can be seen that the spectrometer is divided into two symmetric halves above and below the positron beam pipe. The spectrometer is divided into halves because of the septum plate in the magnet which shields the beams from the magnetic field.

The front or pre-magnet region consists of two high resolution gas microstrip vertex

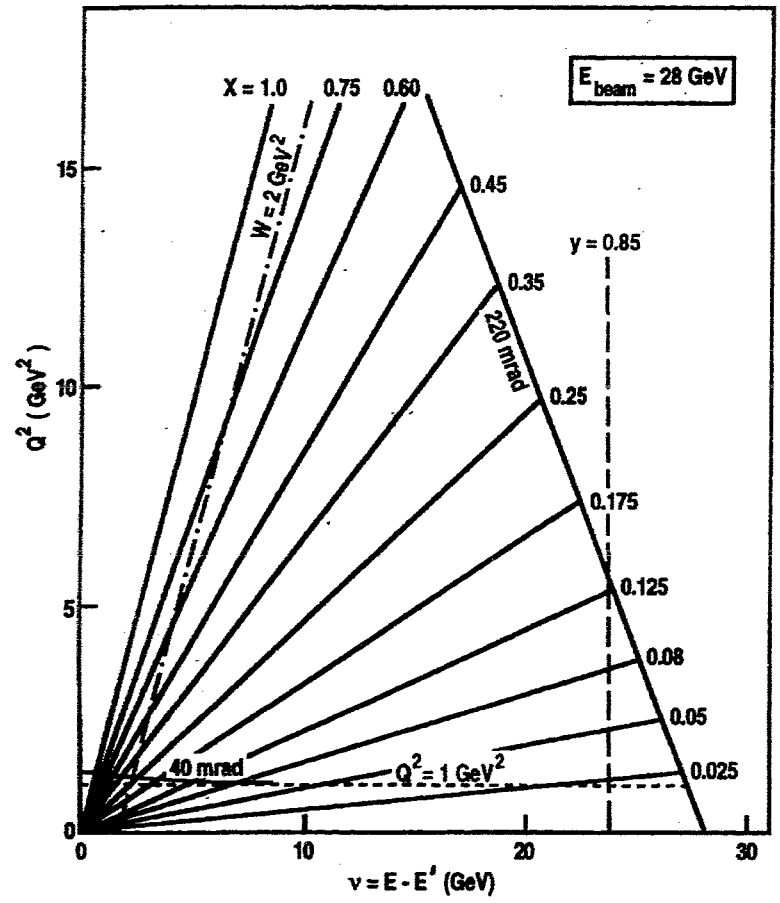

Figure 2.3: The kinematic plane with the HERMES acceptance.

detectors followed by two drift chambers, which measure the position of the scattered particles and thus serve to determine both the interaction vertex and the scattering angle. The four drift chambers in the back region, combined with the pre-magnet detectors and the magnet, complete the measurement of the track momentum by determining the impulse applied to the charged particle by the magnetic field. Three multi-wire proportional chambers are also placed inside the magnetic field to help reduce ambiguities in matching front and back track segments.

The spectrometer has an angular acceptance of $40 < \theta < 220$ mrad, where θ is the scattering angle of the positron. A cut on the invariant mass, $W > 2$ GeV, is necessary to avoid the nucleon resonance region, and Q^2 must be greater than 1 $(\mathrm{GeV/c})^2$ to

interpret the data using the quark parton model. The kinematic plane is given in fig. 2.3 with the above cuts noted. The x range thus accessible to the experiment is $0.02 < x < 0.8$ and the anticipated resolution in x varies from 1% to 8% [6].

A large hadronic background as contamination to the DIS events is anticipated in the HERMES experiment, where, for example, the ratio of pion to positron tracks may be as high as 400 to 1 at low energy and intermediate angles. This contamination arises predominantly from non-DIS photoproduction processes [18], such as $\gamma \rightarrow q\bar{q}$ which couples strongly to the nucleon, as well as from target fragments coincident with DIS events.

Thus, in addition to the need for hadron identification for semi-inclusive measurements, these significant sources of hadronic background motivate the presence of several particle identification (PID) detectors in the HERMES spectrometer. The post magnet region therefore also contains a threshold gas Cerenkov detector, a six module transition radiation detector (TRD), two scintillator hodoscopes, the second of which is preceded by a lead sheet, and a lead-glass electromagnetic calorimeter.

The lead sheet followed by the scintillator counter, which forms a preshower detector, and the calorimeter both take advantage of electromagnetic showers to discriminate positrons from the hadronic background. An electromagnetic shower consists of an initial Bremsstrahlung photon, radiated by a high energy charged particle in matter, which then pair-produces into high energy electrons and positrons. These leptons in turn, as well as the incident particle, will continue to radiate more Bremsstrahlung photons and very quickly an avalanche effect is obtained.

Recalling that the Bremsstrahlung cross section is inversely proportional to m^2, where m is the mass of the incident charged particle, and directly proportional to Z^2, where Z is the atomic number of the material, the lower mass positron is seen to be much more likely than a heavier hadron to cause a shower in the high Z lead [19]. The positron-hadron separation is somewhat reduced however by the additional fact that the hadrons also interact with the nuclei in matter via the strong force, and this interaction may produce a similar avalanche effect, known as a hadronic shower.

The scintillator hodoscope following the lead sheet measures the ionisation radiation in the scintillator material which results from the multiplicity of charged tracks

which make up the avalanche. The lead-glass calorimeter similarly distinguishes the positrons from hadrons by measuring the net amount of this radiation, and in the case of the positron, the shower of which is completely contained by the thick lead-glass, this radiation is proportional to the incident energy. Thus the calorimeter may also be used as a second independent measurement of the positron track energy. The two scintillator hodoscopes and the calorimeter also serve as a first level trigger of the readout electronics for early identification of DIS candidates.

As mentioned in the introduction, the TRD distinguishes particle type based on the emission and detection of transition radiation. The total yield of this radiation depends on the Lorentz factor ($\gamma = E/m$) of the incident particle. Thus the TRD is effective at identifying highly relativistic particles in a relatively compact space which is insufficient for other detector types which depend on differences in β. More detailed information on the theory and design of the HERMES TRD will be presented in the following chapter.

The combined pion rejection power of the above PID detectors in the regime of most significant contamination is anticipated to be of order 40,000 to 1 at 85% positron efficiency, assuming optimal detector performance. However, backgrounds and correlations in the detector responses may reduce the above quoted performance. Fortunately, the anticipated rejection ratio provides a factor of 10 safety margin for an acceptable residual contamination of 1% in the event sample for the asymmetry measurement.

Though the TRD, preshower, and calorimeter serve to discriminate positrons from hadrons, the Cerenkov detector is designed primarily to discriminate pions coincident to the DIS event from the correlated background of heavier hadrons, as required for semi-inclusive measurements of the pion charge asymmetry as well as for unpolarised studies of the flavour asymmetry of the quark sea. The threshold Cerenkov counter detects the characteristic Cerenkov radiation emitted when the velocity of the incident charged particle exceeds the velocity of light in the dielectric gas radiator. Thus, for a given track momentum, the detection of radiation in the Cerenkov detector indicates that the particle mass is below a certain value. The tetrafluoromethane radiator used has thresholds of 4.4, 15.8, and 30.0 GeV/c for pions, kaons, and protons respectively.

Thus, if the TRD, preshower, and calorimeter indicate that the 4.4 – 15.8 GeV/c track was not an electron, the Cerenkov detector will provide identification of pions versus heavier hadrons.

Chapter 3

The HERMES Transition Radiation Detector

The Transition Radiation Detector (TRD) is an essential component of the HERMES particle identification scheme. In the kinematic regime of worst pion contamination, for track energy just above threshold (3.5 GeV) and at intermediate angles (7–8 degrees), the HERMES TRD is anticipated to contribute a pion rejection factor of at least 100:1 at 90% positron efficiency.

The TRD is a relatively recent addition to detector types in High Energy Physics (HEP) experiments. It exploits the Lorentz factor dependence of transition radiation for the identification of relativistic particles. In this chapter the origin and theory of transition radiation will be introduced, as well as the general principles of TRD design. These principles will then serve as the necessary background for a discussion of the design and optimisation specific to the HERMES TRD.

3.1 Transition Radiation Theory

Transition radiation is the electromagnetic radiation emitted as a charged particle traverses an interface between materials with different dielectric constants. Its existence in the optical region was predicted by Ginzburg and Frank in 1946 [20], and later shown by Garibian to extend into the X-ray region in the case of ultrarelativistic

particles where the total energy of the radiation is proportional to the Lorentz factor of the incident particle [21, 22]. The following review derives much of its content from an article by Artru *et al.* [23].

The origin of transition radiation (TR) can be understood more intuitively with the aid of an analogy given by Dolgoshein [24], where the radiation emitted from a charged particle traveling uniformly through a medium of *variable* dielectric constant is compared to bremsstrahlung, the radiation emitted by a charged particle moving *non-uniformly* through a medium of fixed dielectric constant. In particular, in both cases it is the variation of the relationship between the velocity of the particle and the velocity of electromagnetic waves in the medium which accounts for the creation of electromagnetic radiation.

In the relativistic case the total energy of the transition radiation emitted at an interface is proportional to the Lorentz factor $\gamma = E/mc^2$ of the incident charged particle. This feature makes the signature of transition radiation a viable method of particle identification for large values of γ where, for example at 5 GeV, positrons have a γ of order 10^4 and pions a γ of order only 35.

For a single dielectric interface the energy emitted per unit solid angle per unit frequency can be approximated by

$$\frac{d^2W}{d\omega d\Omega} = \frac{\alpha}{\pi^2}\left[\frac{\theta}{\gamma^{-2}+\theta^2+\xi_f^2} - \frac{\theta}{\gamma^{-2}+\theta^2+\xi_g^2}\right]^2, \tag{3.1}$$

subject to the conditions,

$$\gamma \gg 1, \;\; \xi_{f,g}^2 \ll 1, \;\; \theta \ll 1, \tag{3.2}$$

where $\xi = \omega_p/\omega$, ω_p is the plasma frequency, and the subscripts f and g refer to foil and gas, which are the typical nature of the two dielectric media. It can be seen from eq. 3.1 that the radiation is strongly forward peaked in a cone of angle $1/\gamma$.

After integrating eq. 3.1 over angles and frequencies and approximating the gas to have $\omega_p = 0$, the total yield is given by

$$W = 2\alpha\gamma\omega_p/3, \tag{3.3}$$

which exhibits the proportionality to γ mentioned previously and also shows that the number of X-ray photons emitted at a single interface is proportional to $\alpha = 1/137$. Thus in practice multiple interfaces are needed to increase the yield to detectable levels. The theoretical proportionality to γ shown above is limited also in practice by several sources of saturation which are outlined below.

Typically multiple interfaces are achieved by building a stack of foil layers separated by a low density gas or, more ideally, vacuum. Since the plasma frequencies and the Lorentz factor appear only in the combinations $\gamma^{-2} + \xi_f^2$ and $\gamma^{-2} + \xi_g^2$, the simple transformation of variables,

$$\omega'_{Pf} = (\omega^2_{Pf} - \omega^2_{Pg})^{1/2}, \tag{3.4}$$

$$\omega'_{Pg} = 0 \quad (vacuum), \tag{3.5}$$

$$\gamma' = (\gamma^{-2} + \omega^2_{Pg}/\omega^2)^{-1/2}, \tag{3.6}$$

shows that $\gamma' < \gamma$ and $\omega'_{Pf} < \omega_{Pf}$ always hold. Thus use of a gas instead of vacuum can only reduce the net yield. Further, from the above it follows that the plasma frequency of the gas introduces a saturation of the yield when

$$\gamma > \omega/\omega_{Pg}. \tag{3.7}$$

The thickness and spacing of the individual dielectric layers in the stack are constrained by the 'formation zone' lengths whereby the TR yield is significantly reduced if the formation zone thickness drops below a certain minimum. The formation zone lengths $z_{f,g}$ depend on the plasma frequencies of the materials as well as the Lorentz factor of the incident particle and are given approximately by,

$$z_{f,g} = \frac{2}{\omega(\gamma^{-2} + \xi^2_{f,g})}. \tag{3.8}$$

This minimum thickness can be understood as the distance required for the electromagnetic field to redistribute itself. Further, this constraint becomes dominant above some material dependent threshold for the Lorentz factor and thus for a given choice of layer thickness the TR yield will no longer be proportional to the Lorentz factor, but will eventually begin to saturate with increasing γ.

The yield from a stack of multiple dielectric layers introduces a few new effects as well. Foremost, simple self-absorption of the X-rays in the radiator material leads to an obvious saturation of the net yield with increasing radiator thickness, the onset of which depends on the number and thickness of the dielectric layers as well as the density of the materials used. Furthermore, in the absence of regular spacing between layers the analytical determination of the anticipated yield becomes an intractable calculation due to interference effects between layers, in which case numerical evaluation is required to calculate the yield of a given radiator configuration.

3.2 TRD Design Principles

In light of the above, it is clear that the choice of radiator material and layer thickness and spacing requires careful optimisation of a number of factors. Furthermore, the dielectric layers of the radiator are not restricted to being foils spaced in gas, but may consist of dielectric fibres, porous foam, or in fact any light material configuration offering multiple dielectric interfaces. In practice once the experimental constraints are given and the range of interest of the Lorentz factor of the TR emitting (radiating) particle is known, Monte Carlo simulations as well as experimental tests are required to determine the optimal radiator configuration. The design principles outlined below draw heavily from a review article by Dolgoshein [24].

One fairly common design principle which can be deduced immediately from the self-absorption effect mentioned previously is to divide the space available to the TRD into multiple sets of radiator-detector systems, where each individual multi-layer radiator thickness is kept below acceptable saturation levels. This effectively results in multiple statistical measurements of the TR yield.

The task of detecting the TR X-rays is further complicated by the fact that the X-rays are essentially collinear with the incident particle track. Thus the energy deposited by the TR in the X-ray detector, typically a multi-wire proportional chamber (MWPC), is superposed on the ionisation energy loss, or dE/dx, associated with all charged particle tracks. A strong magnetic field could be used to separate the particle track in the downstream X-ray detector from the TR yield, where the mere presence

of energy deposited in the extrapolated detector region is a relatively unambiguous determination of an incident radiating particle, assuming negligible amounts of synchrotron radiation. However, due to typical constraints in spectrometer design such a configuration would be a rare luxury. Thus other techniques have been developed to distinguish the radiating from the non-radiating particle, where the identification of the radiating particle is determined using a probability analysis of the detector response.

There are two principal methods of detector operation used to optimise the identification of the incident particle, namely the cluster counting method and the total energy deposition method. Roughly speaking the former is based on an analysis of the *distribution* of the energy deposited in the detector and the latter on an analysis of the total *amount* of energy deposited in the detector.

The cluster counting method requires fast electronics to resolve localised fluctuations in the distribution of the energy deposited in the detector gas. The characteristic avalanches associated with these local clusters of energy deposition in the detector gas are identified and counted. The principle behind this method is that a TR X-ray will usually deposit all of its energy near the point of absorption. Of course this energy cluster is added to the relatively smooth ionisation energy (dE/dx) along the particle path in the detector gas. Thus the existence of localised clusters of energy above some threshold determined by the typical size of fluctuations in the dE/dx energy distribution is indicative of collinear TR X-ray absorption.

Unfortunately, the rare large fluctuations in the dE/dx may then be mis-identified as the absorption of TR X-rays. These large fluctuations, of order 10–100 keV, are typically due to ionised electrons at large energy transfers, and are called δ-rays for historical reasons. Therefore a probability function must be determined which accounts for the relative frequency of these δ-rays versus the anticipated number of X-rays generated and absorbed in the detector gas for a radiating particle. Note that this method is then optimised by a radiator which produces many TR X-rays with an energy above the energy deposition threshold.

The detection of the characteristic X-ray clusters can be improved by taking advantage of the fact that the X-ray absorption, which decreases exponentially with

distance, is predominant in the first portion of the detector. Thus by using a time-expansion drift chamber with a long drift region followed by anode wires at the back of the detector, the energy deposition from these X-ray clusters can be delayed until the end of the electronic signal and transformed into a time distribution, allowing for enhanced identification since the ionisation fluctuations will be evenly distributed throughout the duration of the signal. Though this time-expansion enhancement decreases the overall spatial requirement for the TRD, the readout electronics required for this method can be, however, prohibitively expensive.

In the total energy deposition method, which is the method chosen for the HERMES TRD, the radiating and non-radiating particles are distinguished by the total amount of energy deposited in the detector. Typical response distributions for this method are given in fig. 3.1. Since the integrated signal for the radiating particle is the sum of the ionisation energy loss plus the energy deposition of absorbed TR X-rays, the total energy deposition method is optimised by a radiator emphasizing the total energy of the TR X-rays rather than the net number as in the cluster counting method. Fig. 3.2 is provided as an example of the impact of the TR energy deposition superimposed on the electron dE/dx in a single module's response. This figure compares the detector responses of 5 GeV electrons with no radiator present (dE/dx only), 5 GeV electrons with a radiator present (dE/dx + TR), and 5 GeV non-radiating pions (dE/dx only). The higher average dE/dx of the electron distribution is a result of the mass-dependent relativistic rise effect. This and other features of the energy deposition in the TRD will be discussed in chapter 5.

The extent to which the overlap of the energy deposition distributions for the radiating and non-radiating particles is minimised is a measure of the rejection power of the TRD. As can be seen from the previous figures, the long high energy tail of the dE/dx distributions for non-radiating particles is the "Achilles' Heel" of this method. In these tail events the occasional high energy δ-ray has deposited a large amount of energy in the detector. The rejection power of the TRD in this method is compromised by these events since a non-radiating particle's total energy deposition becomes comparable to that which is typical of a radiating particle. Consideration of these and other features of the energy loss distributions will be presented in further

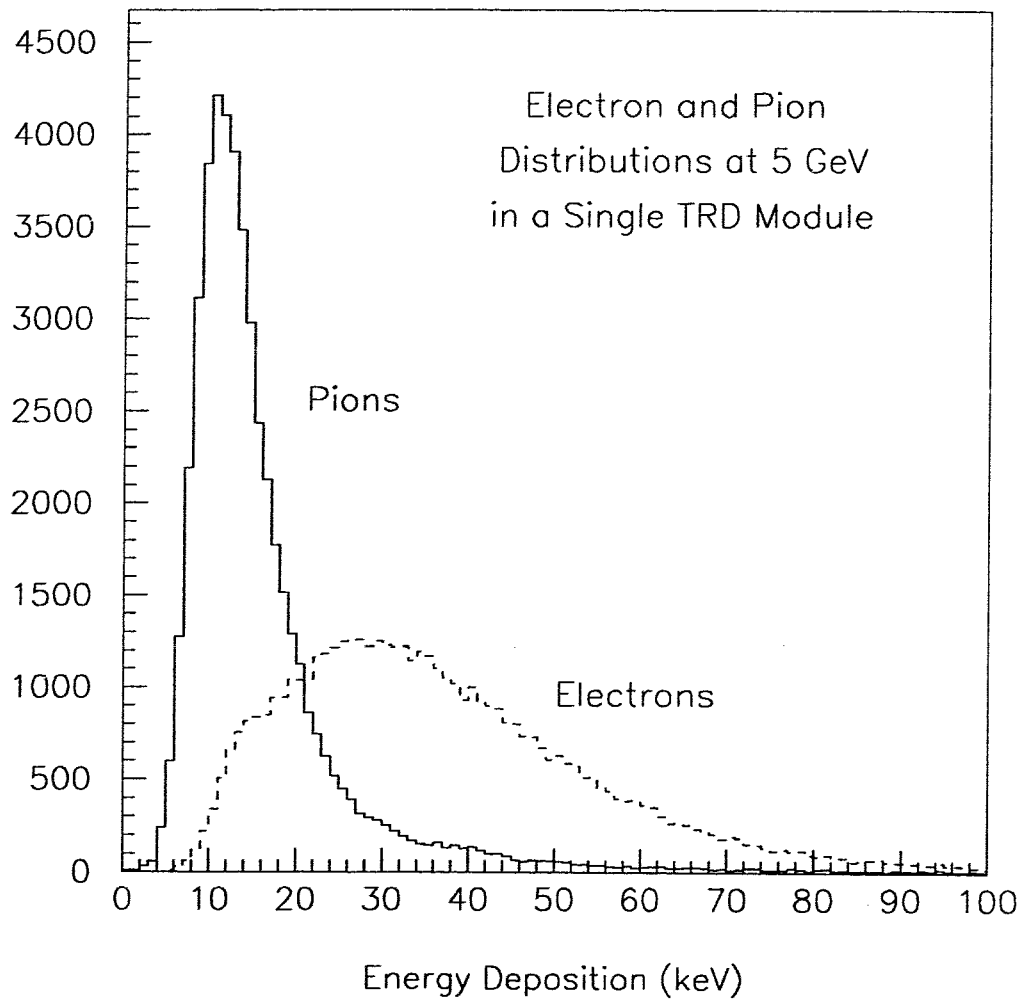

Figure 3.1: Typical response distributions for total energy deposition method. Each distribution contains 50,000 events. The spectra are Monte Carlo simulation results for a single module of the HERMES TRD.

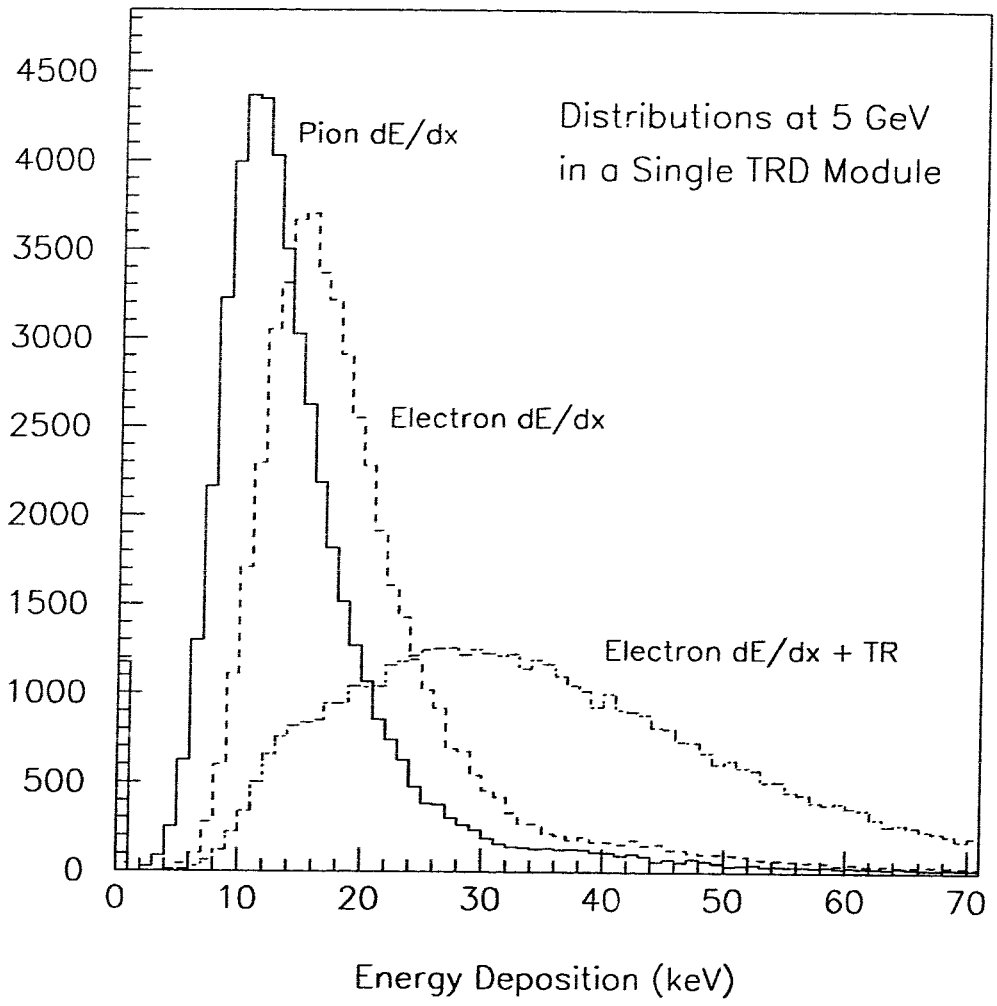

Figure 3.2: Impact of transition radiation on the electron signal.

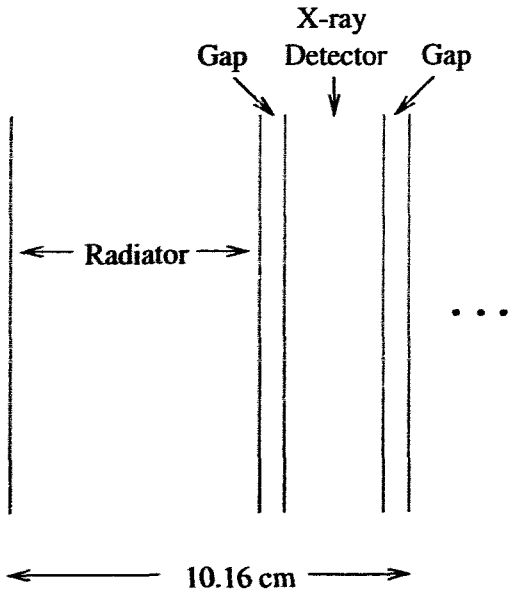

Figure 3.3: Cross section of one physical TRD module. The beam is incident from the LHS and the dots on the RHS denote further modules.

detail in the following section on the HERMES TRD design.

In the total energy deposition method, the probability algorithm used for interpretation of TRD responses to a given experimental event requires use of predetermined total energy deposition distributions for radiating and non-radiating particles, like those given in fig. 3.1. These are typically deduced from either simulation studies or from independent experimental measurements. The methods of probability analysis used for interpretation of the TRD signals will be presented in detail in chapter 6.

3.3 The HERMES TRD Physical Design

The HERMES TRD consists of six modules in each of the lower and upper spectrometer halves. Each physical module consists of a radiator followed by a flush gap, a MWPC as X-ray detector, and then another flush gap. Each TRD half has an active area of 325×72 cm^2. A cross section of one physical TRD module is given in fig. 3.3. The dots denote further modules in series. The basic physical attributes of each of the module's components are presented below.

3.3.1 The Radiator

For optimal TR yield the ideal radiator consists of dielectric layers of regular thickness and regular spacing at the respective minimum formation zone lengths of the material and of the gas. Since X-ray absorption goes as Z^4, for minimum self-absorption the dielectric material should have the lowest possible Z and maximum plasma frequency, or equivalently maximum electron density, with the dielectric layers separated by a gas of lowest possible Z, or, more ideally, vacuum [24]. Due to the practical constraints involved in the construction of such an ideal radiator, various alternative radiator configurations have been developed, all sharing of course the key feature of multiple dielectric transitions.

Some of these competing radiator types were tested with a TRD prototype. In particular a pseudo-ideal radiator of quasi-regularly spaced foils and various types of foam were compared to fibre materials. The performance of the fibres proved sufficiently competitive to warrant their use from considerations of convenience, cost, and reliability [6]. The loosely packed cylindrical fibres approximate the ideal case of foil layers of regular thickness. The fibre diameter and radiator density were optimised with the aid of Monte Carlo simulation of the TRD.

The above studies resulted in a choice of radiator material consisting of 17 micron diameter polypropylene (CH_2) fibres with air at NTP as the second dielectric. The radiator material has a net density of 0.059 g/cm^3. Thus each 6.35 cm radiator consists of roughly 267 dielectric layers. The distribution of fibres within the radiator is non-heterogeneous and irregular. The fibres are matted in 2-dimensional layers in the x-y plane (transverse to the beam direction), but these matted layers are then quasi-randomly distributed along the z (beam) direction.

3.3.2 The X-ray Detector

The TR X-ray yield from each radiator incident upon the MWPC is typically of order 2–3 photons predominantly in the energy range 5–10 keV. A 90:10 Xe/CH_4 gas mixture is used in a 2.54 cm thick MWPC. The thickness of 2.54 cm is a convenient length which maximises X-ray absorption in xenon while minimising the dE/dx ionisation

energy loss.

The xenon gas is chosen over other noble gas candidates such as argon or krypton because of its efficient absorption of X-rays in the relevant TR energy range, low energy fluorescence from the L-shell at 5.5 keV, and consequent high ratio of X-ray absorption to ionisation energy loss per unit length. Furthermore, the relativistic rise, or increase in the average dE/dx of the radiating positron over that of the non-radiating pion of the same momentum, is greater in xenon than other noble gas candidates. These and other characteristics of energy loss will be discussed in more quantitative detail in chapter 5.

CH_4 is added as a quench gas to maintain the stability of the proportional chamber. During the multiplication avalanches in the high fields near the anode wire fluorescent UV radiation is emitted. If this radiation reaches the cathode foils it may then eject electrons by the photoelectric effect. These electrons then drift back to the anode leading to an unstable positive feedback mechanism. The role of the CH_4 is to quench this process by efficiently absorbing the fluorescent radiation via the many vibrational modes which result from its molecular structure.

Since minimising cost rather than space was a primary concern, the total energy deposition method was chosen. Thus the particle gamma is distinguished based on multiple measurements of the total energy deposited in each module for a given track.

The MWPC has anode wires spaced every 1.27 cm. This wire spacing is a trade off which minimises cost while reducing the impact of the energy loss in a given wire cell from δ-rays and hadronic 'showers' produced in the radiators. Though δ-rays are predominantly ejected perpendicular to the incident particle track, through multiple scattering their direction is quickly randomised and the finest possible wire spacing minimises the likelihood of δ-rays wandering into the struck wire cell. The wire spacing also minimises the energy deposited in a given wire cell by large energy transfer δ-rays emitted in the detector gas itself.

In the case of hadronic 'showers', which expression refers to the few secondary hadrons generated from a hadronic interaction, minimal wire spacing reduces the geometrical acceptance of each wire cell and thus reduces the number of secondary tracks which traverse the cell struck by the primary track. Noting that the summed

ionisation signal from multiple secondary hadron tracks is easily mis-identified as that of a radiating particle, for which the dE/dx ionisation and TR X-ray absorption are summed, and also noting that a hadronic 'shower' initiated in one of the first radiators may induce mis-identification in many of the remaining modules, the importance of reducing sensitivity to these secondary hadron tracks becomes evident.

3.3.3 The Gas System and Flush Gaps

Due to the high cost of xenon a rather sophisticated gas system has been developed to recirculate the xenon gas mixture as well as remove gas impurities which compromise detector performance. The gas system also monitors and maintains the differential pressure between the X-ray detector and the flush gaps.

The primary motivation for the gas system and flush gaps is to protect the Xe/CH_4 gas mixture from diffusion of impurities, such as the nitrogen, oxygen, and water vapour, through the mylar foil. CO_2 was chosen as the gap gas because it is relatively transparent to X-rays, inexpensive, and also a comparatively easy gas impurity to remove from the Xe/CH_4 gas mixture.

A second role of the gas system and the pressure-controlled flush gaps is to stabilise the aluminised mylar cathode foils which define the X-ray detector gas volume in order to keep gain fluctuations within a 1% tolerance. This requires maintaining the differential pressure across the foil stable to less than 1 part in 10^5, or equivalently, stabilising the foil position to within 0.01 mm.

Chapter 4

TRD Prototype Tests

Test experiments using a single TRD prototype module were performed in a CERN test-beam in both 1991 and 1992. In the 1992 experiment, the results of which will be presented below, the TRD response to various radiator types was measured for pions and electrons in the energy range from 5 to 50 GeV. The five radiator types tested were a foil radiator of quasi-regularly spaced foils, 2 fibre radiators with fibre diameters of 17–20 and 25–30 micron diameters respectively, and 2 types of foam radiator.

Unfortunately the sample radiators were not prepared in an optimal manner for direct experimental comparison. These experimental test results were nonetheless vital for two reasons: first they provided important evidence that the 'fibre' radiators, preferred for the practical reasons outlined earlier, would meet the pion rejection factor (PRF) design requirement, and second, the experimental results provided an essential check on the accuracy of the Monte Carlo simulation and standard for its fine-tuning. In particular, the Monte Carlo simulation had already predicted that the 17–20 micron fibre radiator would perform adequately. The experimental tests were nonetheless necessary to confirm the reliability of the simulation results which would be used to optimise the final design through studies of the performance of the correlated six module TRD.

In this chapter the method of analysis of each radiator's performance is reviewed,

followed by a discussion of the specifications and measured performance of each radiator type. First, however, a brief overview of the experimental setup is presented.

4.1 Overview of Test Experiment

The test experiment was performed in the X3 test beam line at CERN. The pions and electrons of varying energy were tertiary particles produced from the protons of the Super Proton Synchrotron (SPS) as follows. The SPS protons were directed into a target which produced secondary pions in the H3 beam line. The resulting pion beam was directed into a second target the nature of which depended on the final particle type requirement for a given run. For a pure electron beam a lead target was used and for a mixed beam either a copper or beryllium target was used. For a pure tertiary pion beam a 5 mm lead absorber was added downstream of the copper or beryllium target. The resulting tertiary pions and electrons were then momentum selected by a combination of sweeping magnets with collimators.

The final particles were identified using two upstream threshold Cerenkov detectors which provided independent identification of the particle type. In addition to the Cerenkov detectors there were five upstream scintillators used for event triggering. Finally, the radiator types under study were rotated on an automated wheel in front of the TRD flush gap.

4.2 Method of Analysis

In this section the basic principles and terminology of the method that will be used for quantitative measure of each radiator's performance are introduced. In particular, the figure of merit is the pion rejection factor (PRF) of each radiator-detector system at a given electron efficiency. The pion rejection factor is a measure of the ability of the detector to discriminate non-radiating pions, with a Lorentz factor of roughly 35 at 5 GeV, from the TR emitting electrons, with a gamma of order 10^4 at 5 GeV.

Recalling that in the total energy deposition method radiating and non-radiating particles are discriminated based on the net energy deposited in the detector, the

electron efficiency represents the percentage of electron events which deposit a net amount of energy greater than some energy deposition threshold. Thus once an acceptable electron efficiency is determined, the energy threshold which provides this efficiency is fixed. The PRF then represents the ratio of the total number of pion events to those that deposit more energy in the detector than this threshold. Thus the PRF is a measure of the number of pions which would be mis-identified as electrons, or equivalently, a measure of the pion contamination, when the particle identity is not known *a priori.*

The results for the five different radiator types and densities will be presented in terms of an extrapolated six module truncated mean. 'Truncated' denotes that the highest individual module result is excluded from the mean and 'extrapolated' is a reminder that six separate events with the same particle type in a single module are being used rather than six successive module responses to the same particle. Hereafter the qualifier 'extrapolated' will be implied when referring to the prototype TRD results.

The motivation for the six module comparison is to ascertain the PRF performance of the actual six module HERMES TRD. The extrapolation to six modules is of course limited in accuracy since correlation effects between the six TRD modules are neglected. Further, the existence of different correlated and uncorrelated background sources between the experimental environments at CERN and within the HERMES spectrometer at HERA also limit the predictive power of these experimental tests.

In fig. 4.1 the impact of the truncated mean method on the distributions is presented in comparison to the simple untruncated six module mean. This figure offers a qualitative picture of how the high energy pion tail of the simple mean is reduced by the truncated mean algorithm. The effect of truncation on the electron spectrum is also shown for comparison.

The basis for the truncated mean method is to preferentially reduce the effects of large energy transfer δ-rays generated in the radiator and detector gas, noting that high energy δ-rays are created fairly infrequently. In particular, the probability of an

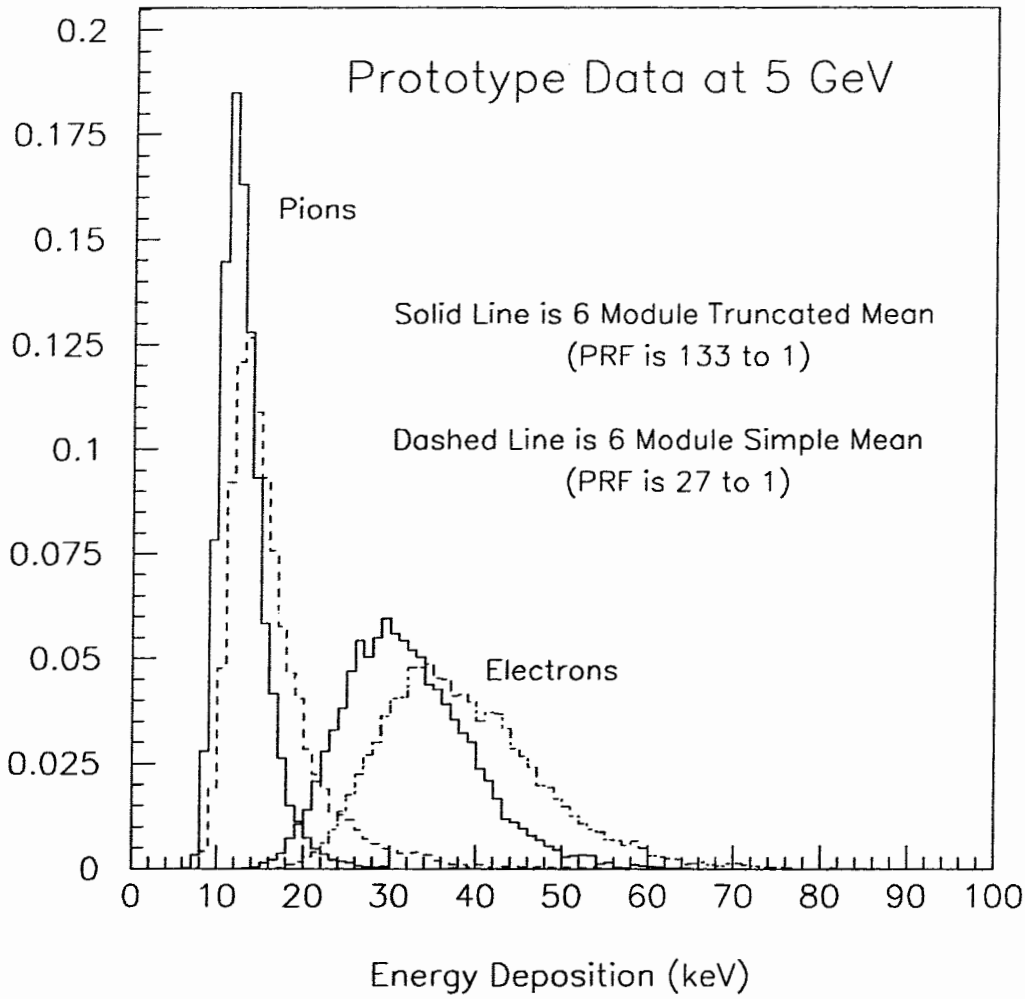

Figure 4.1: Comparison of distributions for truncated and simple mean algorithms using 17 micron fibre radiator data.

electron being ejected with energy E can be approximated by [25],

$$P(E) \approx K\frac{Zx}{\beta^2 AE^2}, \tag{4.1}$$

where x is the reduced thickness of the medium in g/cm^2, $K = 0.154$ MeV g^{-1} cm^2, and $\beta = v/c$. Thus the number of δ-rays produced above a threshold E_o can be approximated by,

$$N(E > E_o) \approx \frac{KZx}{\beta^2 AE_o}. \tag{4.2}$$

Using the above formulae the impact of truncation on the PRF can be crudely estimated. Consider the simple mean distribution given in fig. 4.1: the pion spectrum is peaked at roughly 15 keV and the electron spectrum at roughly 35 keV. The minimum energy of a single δ-ray contaminating one module which, when averaged over six modules, would induce mis-identification of a pion as an electron is roughly 100 keV, assuming also that the responses of all other modules to this pion event average to the 15 keV peak of the pion spectrum. Subject to the above caveat, a calculation using eq. 4.2 gives of order a few percent of pion events will have δ-rays ejected with an energy greater than 100 keV in the combined thickness of six gas detectors (neglecting also radiator δ-rays which penetrate into the gas.) This means a few extra pion events out of every 100 would be mis-identified as electrons due to these high energy δ-rays. It is precisely these events which are preferentially discarded by the truncated mean method.

On the other hand, the negative impact of rejecting the greatest TR + dE/dx yield for the radiating particle in a single module has also been neglected in the above estimate. It is, however, much more difficult to estimate the extent to which this negative impact on the electron distribution offsets the benefits from eliminating a large fraction of the contaminating large energy transfer δ-ray events. The net effect on the PRF can only be determined empirically using either experimental results or Monte Carlo simulation. Using the 17 micron fibre radiator data the pion rejection factors were calculated for the simple and truncated mean distributions given in fig. 4.1. The pion rejection factors are 27:1 and 133:1 for the simple and truncated mean respectively. Thus the relative improvement of the PRF is in accordance with the rough

estimate obtained above, where a few contaminating events for every hundred have been eliminated.

4.3 Results of Analysis

The five radiator types tested at CERN all diverged from the ideal radiator in different ways and degrees. These five radiator types consisted of: 1) a foil radiator of quasi-regularly spaced foils, 2) two fibre radiators with fibre diameters of 17–20 and 25–30 microns respectively, and 3) two types of porous foam. Given that both the space allocated for the TRD and the maximum number of TRD modules were both relatively inflexible constraints, the performance of the competing radiators would be most fairly compared at similar thicknesses, and ideally at the thickness prescribed by the above constraints. Since some of the samples available at the time had different thicknesses, the fairest possible comparison would then require extrapolation with simulation for any radiator types that proved competitive with the preferred 17 micron fibre radiator.

4.3.1 The Fibre Radiators

The preferred 17–20 micron polyethylene fibre radiator was prepared with the required thickness of 6.35 cm, imposed by TRD design constraints, and a net density of 0.101 g/cm^3. Since the fibres are cylindrical and predominantly transverse to the beam direction, the average thickness of a fibre, or 'foil' layer, traversed by an incident particle is 13.4 microns. This gives roughly 477 dielectric layers. The six module truncated mean for this radiator is given in fig. 4.2, and, at 90% electron efficiency, yields a PRF of 133:1. The electron efficiency threshold, or particle identification (PID) cut, is indicated by a vertical line.

The extrapolated PRF for the preferred 17–20 micron fibre radiator thus fulfills the design requirement for the six module TRD. However, as mentioned previously, this 'extrapolated' truncated mean neglects the impact of correlations between the six modules of the TRD, which would reduce the anticipated performance. The studies with Monte Carlo simulation of the HERMES TRD which included these correlations

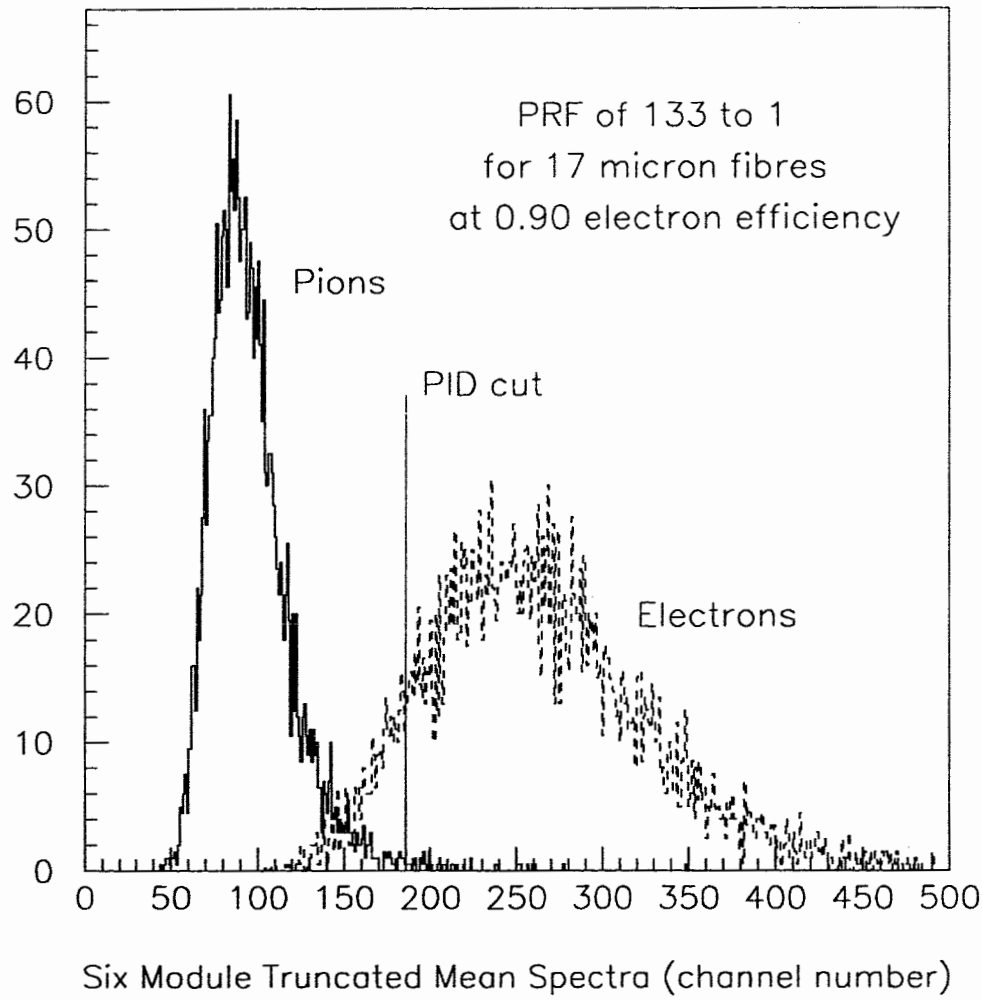

Figure 4.2: 17–20 μ fibre radiator: six module truncated mean at 5 GeV. The electron efficiency threshold (PID cut) is indicated by the vertical line.

as well as other second order effects will be discussed in the following chapter.

The six module truncated mean spectra for the 25–30 micron fibre radiator are presented in fig. 4.3, although the radiator sample thickness of 3.6 cm is too short for direct comparison to the 17-20 micron fibre radiator. As noted in the figure, the PRF at 90% electron efficiency for this radiator sample is 39:1.

4.3.2 The Foil Radiator

The quasi-ideal foil radiator had a thickness of 7.29 cm with a density of 0.092 g/cm^3. Though this radiator was designed to have 15.2 micron foils, regularly spaced by 141 micron gaps, the prototype construction method proved difficult and the 467 foils lacked sufficient tension to maintain their designed spacing. Nonetheless the six module truncated mean for this foil radiator is still of comparative interest and the spectra for 5 GeV pions and electrons are presented in fig. 4.4. The PRF at 90% electron efficiency for this radiator is 130:1. Thus the quasi-ideal radiator and the 17-20 micron fibre radiator are seen to perform comparably.

4.3.3 The Foam Radiators

Two types of porous polyethylene foam were tested at CERN. The first of these (R-foam) was obtained from Russian colleagues (hence the name) and had a thickness of 7.62 cm. The second (H-foam) was also 7.62 cm thick. The truncated mean spectra for the R-foam and H-foam are presented in fig. 4.5 and fig. 4.6 respectively. The PRF at 5 GeV for the H-foam is 59:1 and for the R-foam is 46:1. Thus in spite of the additional length neither radiator type is competitive with the 17–20 micron fibre radiator.

4.3.4 Summary of Results

The PRF results of the competitive fibre and foil radiators, all at 90% electron efficiency, are collected in table 4.1 for convenient reference. The thicknesses and densities of these samples are also noted in the table.

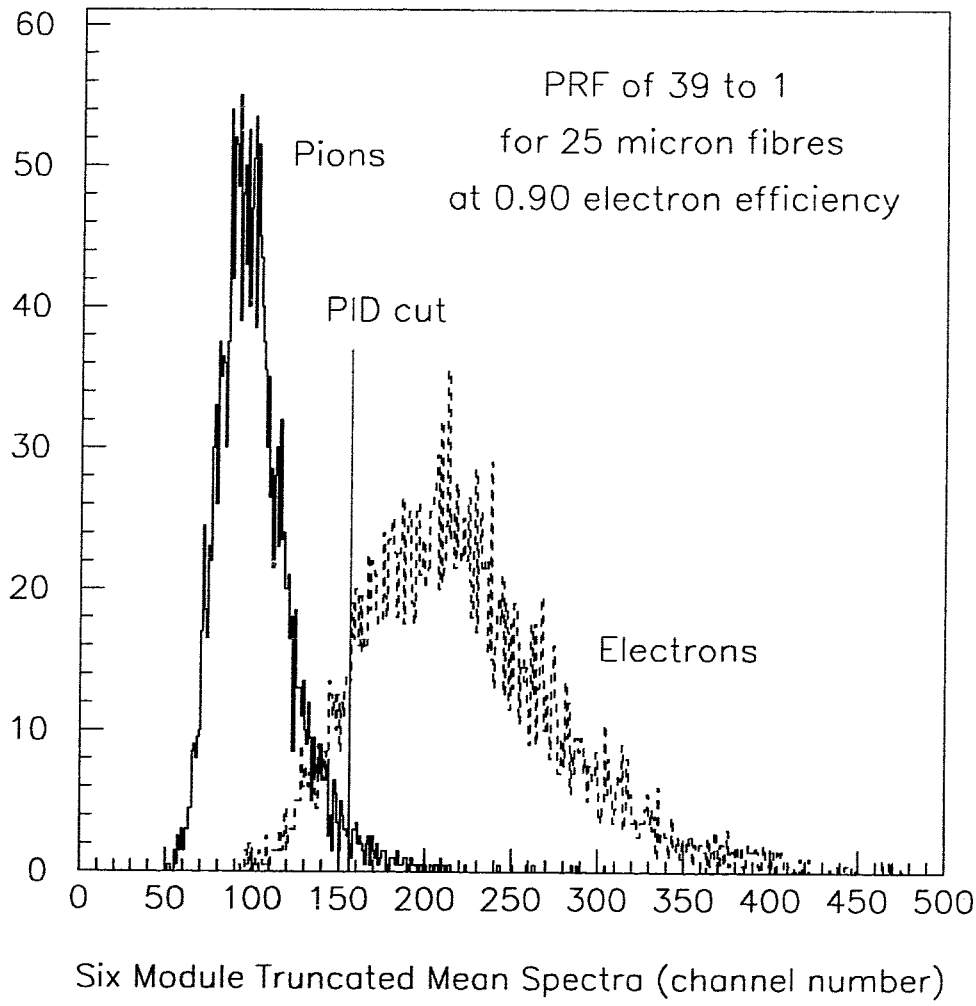

Figure 4.3: 25–30 μ fibre radiator: six module truncated mean at 5 GeV. The electron efficiency threshold (PID cut) is indicated by the vertica line.

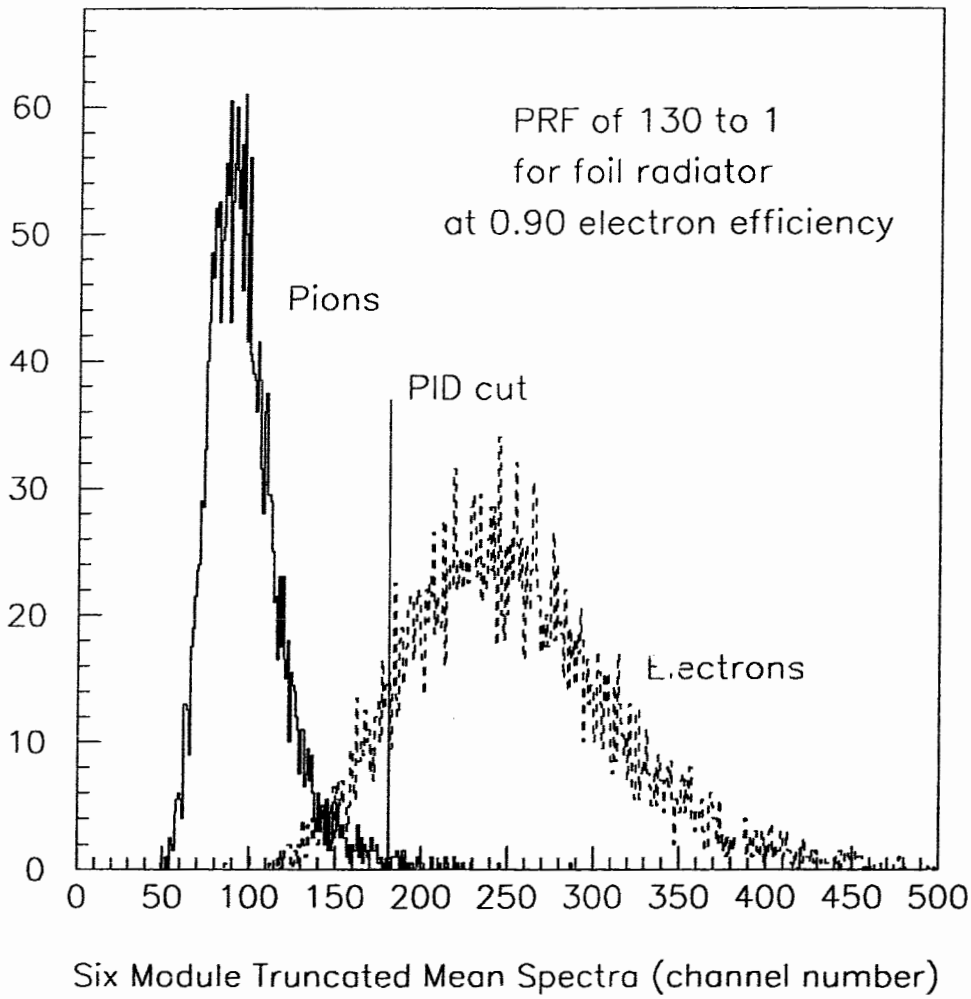

Figure 4.4: Quasi-ideal μ foil radiator: six module truncated mean at 5 GeV. The electron efficiency threshold (PID cut) is indicated by the vertical line.

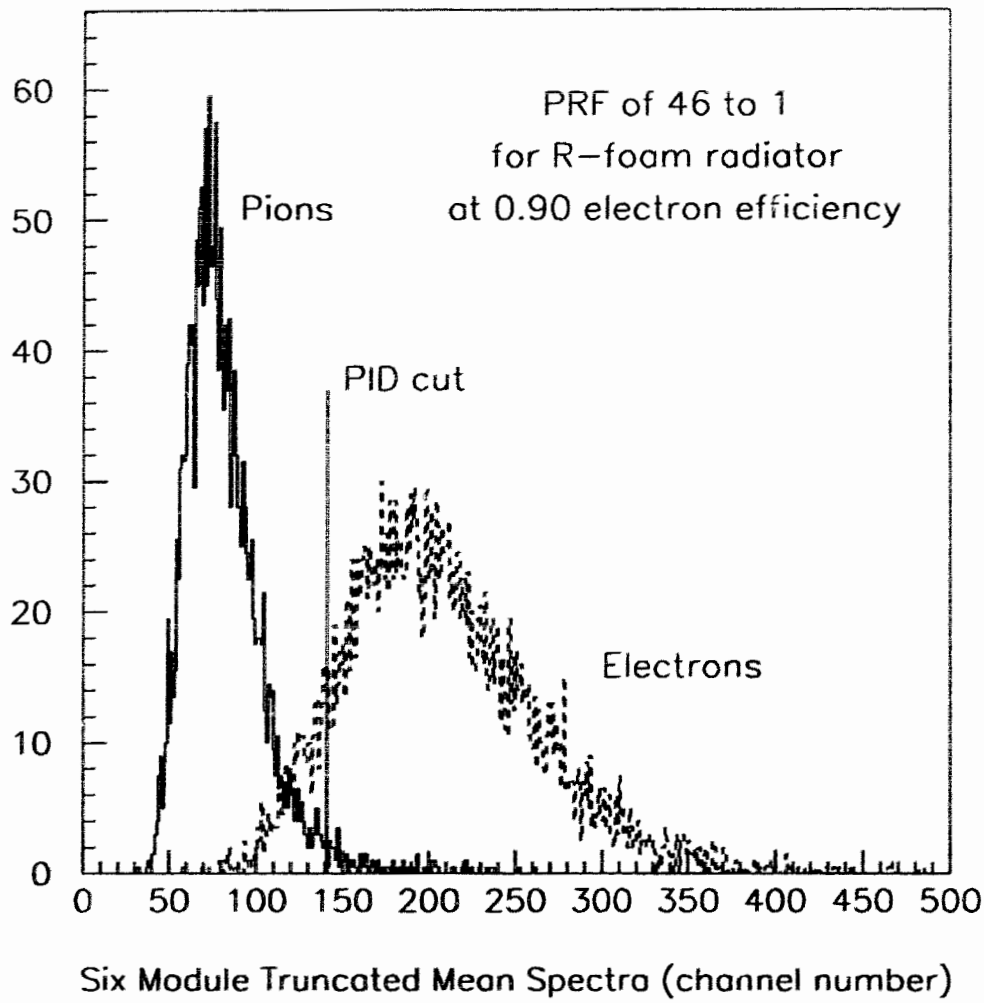

Figure 4.5: R-foam radiator: six module truncated mean at 5 GeV. The electron efficiency threshold (PID cut) is indicated by the vertical line.

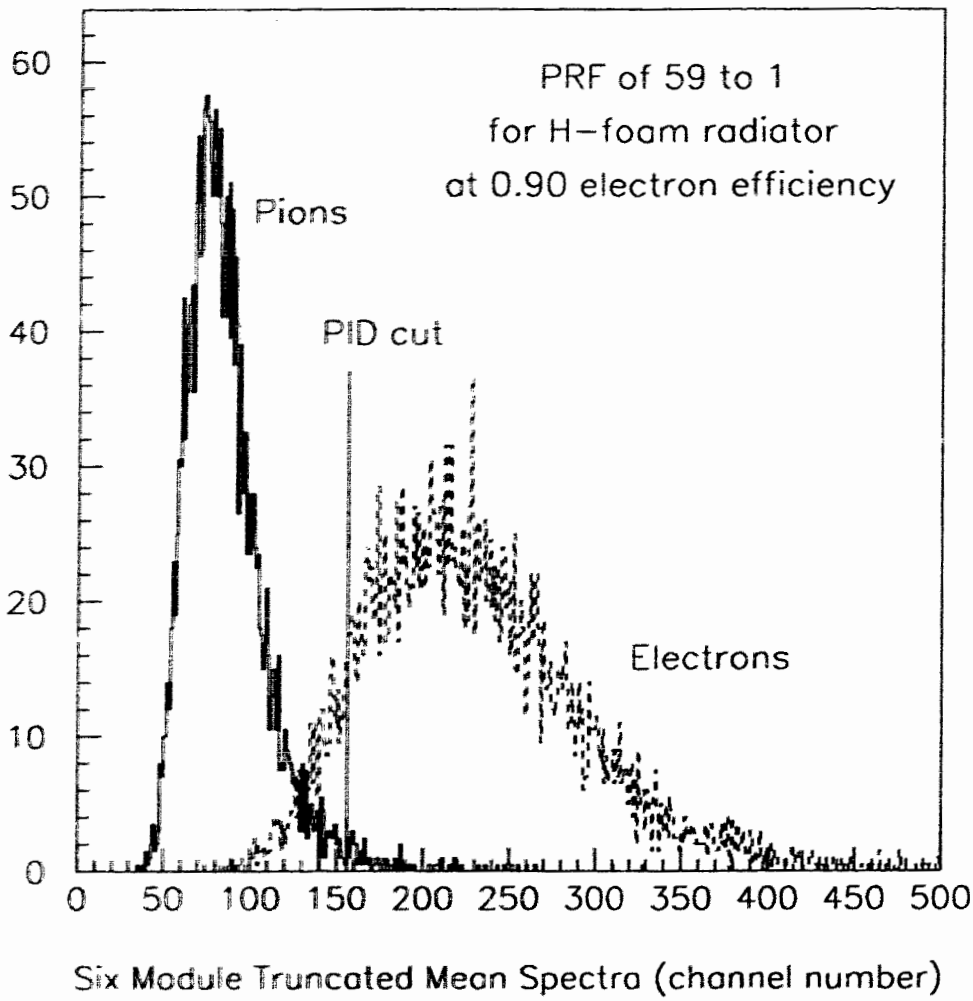

Figure 4.6: H-foam radiator: six module truncated mean at 5 GeV. The electron efficiency threshold (PID cut) is indicated by the vertical line.

Table 4.1: Summary of the PRFs for each of the radiator types tested.

Radiator Type	Thickness (cm)	Density (g/cm^3)	PRF
17–20 μ Fibres	6.35	0.101	133:1
15.2 μ Foils	7.29	0.092	130:1
25–30 μ Fibres	3.6	0.18	39:1

In summary, the experimental tests established that, to first order, the 17–20 micron fibre radiators generated sufficient net TR yield for the six module HERMES TRD to achieve the required pion rejection factor in the space allotted. This experimental result confirmed the adequacy of this radiator type as anticipated by Monte Carlo simulation. Furthermore, these experimental results provided an essential check on and standard for the fine-tuning of this Monte Carlo simulation which was used as a tool in developing the final detector design. The experimental results also served as a standard for the later Monte Carlo simulation which superseded the original simulation. The comparison of the new simulation with experimental data and the motivation for its development are provided in the following chapter.

Chapter 5

Monte Carlo Simulation of the TRD

Monte Carlo simulation in high energy physics (HEP) consists of random numerical sampling of the relevant physics cross sections for particles with defined kinematics as they are tracked through a geometrical representation of the detector media. It is from this random sampling process that the Monte Carlo method of numerical evaluation derives its name. Due to the ever increasing complexity of HEP detectors and experiments, Monte Carlo simulation has become an important tool not only for detector design but also for the optimisation of detector performance and the interpretation of experimental results.

In the first section of this chapter, the uses of Monte Carlo simulation for the HERMES TRD specifically as well as for the complete HERMES experiment will be introduced and motivated. After a detailed review of the processes of energy deposition most relevant to the performance of the TRD, the methods of numerical evaluation of these and other secondary processes will be discussed in detail in parallel with the description of the final TRD Monte Carlo simulation. The simulation results will then be shown to be in good agreement with the experimental test data presented in the previous chapter. In the final section of this chapter the Monte Carlo studies of the variation of the TRD response under the range of kinematic conditions will be presented. The particle identification algorithms which use these TRD response

distributions to interpret the TRD data will be reviewed in the final chapter.

5.1 Overview and Motivation

Monte Carlo simulation is essential for TRD design due to the analytical intractability of radiator performance and the limited opportunity and finances to experimentally test the numerous design possibilities. Thus a Monte Carlo simulation of the TRD was developed during the design period. Due to the unavailability at the time of a single detector simulation package which had proven itself adequate to accurately simulate all the various low energy physics processes which strongly influence the TRD performance, this first simulation combined the strengths of various simulation packages and algorithms in order to maximise its accuracy.

The above 'hybrid' simulation was later supplanted by an independent and improved Monte Carlo simulation which was developed *after* the design period. The second simulation was based almost exclusively on a detector simulation package called GEANT [26]. This new GEANT based TRD simulation was developed for two reasons. The first of these was to develop, test, and optimise TRD algorithms which would be needed for the GEANT based Monte Carlo of the entire HERMES experiment. The second purpose was to efficiently generate anticipated TRD responses under a variety of experimental conditions for use in the event reconstruction software.

The GEANT simulation tools had been chosen as the basis for the HERMES Monte Carlo (HMC) simulation of the entire HERMES experiment. Hence use of the GEANT package for those algorithms relevant to simulating the TRD response within the HERMES spectrometer would greatly facilitate integration of the TRD subroutines into the HMC simulation. A GEANT based simulation of the *prototype* TRD was thus first developed to test if the GEANT algorithms could reproduce the available experimental data. The extent to which the GEANT tools proved adequate avoided the difficulties involved in combining various other simulation packages or in developing new physics simulation algorithms. The relevant subroutines and optimised parameter settings of this GEANT based *prototype* TRD simulation could then be easily adapted to the simulation of the HERMES TRD and efficiently included

into the HMC simulation.

The second purpose mentioned above was the generation of statistical distributions of energy deposition in the TRD under the range of kinematic conditions; that is, under the various possible combinations of incident particle type, energy, and track angle. These simulated response distributions are needed for interpretation of the TRD data. This need for accurate simulated data is somewhat unique to the particle identification detectors. In the TRD, for example, knowledge of the anticipated response distributions is in fact necessary to extract the *probabilities* that a particular response in the TRD was caused by each of the particle type candidates, as will be explained in detail in the following chapter. The use of simulated data for this end is necessary only until sufficient data has been collected by a well-calibrated spectrometer to provide the real distributions with good statistical precision.

5.2 Theory of Energy Loss

This review of the physics of energy loss owes much of its substance to a report by Sauli [25] on the energy loss processes in gas detectors. It is divided into two separate subsections for each of the two primary mechanisms of energy loss. The first of these deals with ionisation energy loss by charged particles and the second with the absorption of X-ray radiation.

For the special case of a TRD, in the comparatively dense radiator material which consists of multiple dielectric transitions, a very small contribution to the energy loss is from the creation of transition radiation (TR). Though the theory of TR has already been presented in a previous chapter, the method of *numerical* evaluation used in the TRD simulation for this extremely relevant form of energy loss will be presented in the section on the description of the Monte Carlo simulation.

5.2.1 Ionisation Energy Loss

The dominant mechanism of energy loss for charged particles in gas detectors is through excitation and ionisation of the atoms of the medium. The theoretical expression for the average energy loss per unit length was derived by Bethe and Block and is given by [25] ,

$$\frac{dE}{dx} = -K\frac{Z}{A}\frac{\rho}{\beta^2}\left[\ln\frac{2mc^2\beta^2E_{max}}{I^2(1-\beta^2)} - 2\beta^2\right], \tag{5.1}$$

where,

$$K = \frac{2\pi N_A z^2 e^4}{mc^2},$$

Z, A, I, and ρ are the atomic number, atomic mass, ionisation potential, and density of the medium respectively, and z and β are the charge and velocity of the incident charged particle. E_{max} is the maximum energy transfer allowed in a given interaction and is given by,

$$E_{max} = \frac{2mc^2\beta^2}{1-\beta^2}. \tag{5.2}$$

From the above equation it can be seen that the average energy loss will decrease with increasing particle velocity until some minimum value, referred to as 'minimum ionising' energy loss. Eventually however the logarithmic term begins to dominate and leads to an increase in the energy loss with increasing particle velocity. The onset of this 'relativistic rise' is mass dependent.

However, in the case of the TRD, it is the *distribution*, rather than the *average*, of the energy loss which is of even greater interest since the detector performance depends critically on the overlap between the distributions of the radiating (dE/dx + TR) and non-radiating (dE/dx only) particle types. The well-known asymmetric distribution Landau has derived for the energy loss fluctuations is given by,

$$f(\lambda) = \frac{1}{\sqrt{2\pi}}\exp\left\{-\frac{1}{2}[\lambda + \exp(-\lambda)]\right\}, \tag{5.3}$$

where λ is given by,

$$\lambda = \frac{\Delta E - \Delta E_{mp}}{\xi}. \tag{5.4}$$

Here ΔE_{mp} is the most probable value of energy loss, and ΔE is the actual energy loss for a given event.

The derivation for the Landau distribution of the energy loss is subject to the conditions:

$$\xi/E_{max} \ll 1, \tag{5.5}$$

$$\xi/E_o \gg 1, \tag{5.6}$$

where,

$$\xi(MeV) = 0.1536(Z/A)\rho x/\beta^2. \tag{5.7}$$

Here x is the thickness of the medium in cm, ρ the density in g/cm^3, and E_o is the typical electron coupling energy in MeV. The second condition (eq. 5.6) of the derivation corresponds to the assumption that there are many small energy transfer collisions in the medium, allowing their contribution to the fluctuations to be ignored. This equates to a detector thickness requirement [27]:

$$x \gg 2\beta^2 Z, \tag{5.8}$$

which fails in the case of a 2.54 cm Xe/CH_4 detector.

Though the Landau theory offers insights into the quantitative evaluation of energy loss fluctuations, the deviation of experimental results from the Landau distribution in the case of very thin absorbers limits its usefulness in describing energy loss in the thin gas layers which characterise proportional chambers, where the width of the distribution of energy loss is much broader than predicted by Landau theory. On the other hand, as will be seen below, methods of *numerical* evaluation have been developed which overcome the constraint of eq. 5.6 in the calculation of the fluctuations in energy loss in very thin absorbers.

5.2.2 Absorption of X-ray Radiation

The attenuation of electromagnetic radiation in a medium of reduced thickness x (in g/cm^2) can be written as,

$$I(x) = I_o \exp[-\mu x], \tag{5.9}$$

$$= I_o \exp\left[\frac{-x}{\rho\lambda}\right]. \tag{5.10}$$

Here μ is the mass attenuation coefficient, ρ is the medium density, and $\lambda = (\mu\rho)^{-1}$ is the mean absorption length.

In the soft X-ray range of the electromagnetic spectrum, corresponding to the detectable transition radiation, the dominant contribution to the attenuation is from the photoelectric effect. In this process an electron of energy E_e is ejected from an atomic or molecular shell of binding energy E_j through the absorption of a photon of energy $E_\gamma = E_j + E_e$. Thus the energy loss from the photoelectric effect is a discrete localised event in contrast to that of ionisation.

After photoelectric absorption the atom or molecule will then de-excite primarily through either the Auger effect or fluorescense. In the case of the Auger effect the remaining bound electrons de-excite through radiationless transitions resulting in the emission of another electron with energy just less than E_j. Through this process nearly all of the incident X-ray energy is converted into electron kinetic energy.

The other mechanism of de-excitation is fluorescence, in which case a photon of energy $E_f = E_j - E_i$ is emitted during an electron transition from the ith to the empty jth shell. The fluorescent photon will then have a much larger mean free path since its energy E_f is just below the jth absorption edge. This effect is important to take into account since a large fraction of this fluorescent energy will in fact escape the detector gas totally. The percentage of events involving fluorescence, rather than Auger transitions, is called the fluorescent yield.

5.3 Description of the Monte Carlo Simulation

This section will focus on the description of the GEANT based simulation which superseded the earlier hybrid simulation in accuracy. Unless otherwise stated, hereafter 'TRD simulation' refers to the GEANT based simulation.

The version of GEANT available at the time officially claimed to reproduce to within a few percent all electromagnetic energy loss processes for particle energy down to 10 keV [26]. Unofficially, however, the latest version of GEANT had been

recently extended to include energy loss down to 1 keV [28], which is necessary for correct simulation of TR photoabsorption. As mentioned above, the TRD simulation was developed to test if these new GEANT algorithms could perform adequately, or, more specifically, to determine which, if any, of the various alternative models of energy loss in GEANT most relevant to the performance of the TRD could accurately reproduce energy loss in the TRD gas down to the few keV range.

Though the focus below will be on models of electromagnetic ionisation and photoabsorption, there are many other physics processes of secondary importance to the simulation. The accuracy of the GEANT models for these processes is not as critical as for the physics processes outlined above. In principle the default GEANT parameters and models for these second order effects in the TRD simulation were tested *implicitly* in the final comparison to the experimental data.

The algorithm for the detector simulation can be broken down into the following components: definition of the geometry and materials; initialisation of cross section tables; generation of incident particle kinematics; transport, or tracking, through the geometry of these particles and any secondaries generated; numerical sampling of the physics processes affecting the particles in the successive media; and evaluation, or digitisation, of the energy deposited in the detector volumes.

For the TRD simulation of the test experiment, the TRD itself and the five upstream scintillator counters were included in the geometrical representation. The scintillator material was included in light of its small but important contribution to generating hadronic 'showers' which contaminate the pion distribution. The 1 cm thick scintillator counters were positioned 23.5, 38.8, 50.8, 109.8, and 126.8 cm upstream from the center of the TRD.

The initial kinematics of the pions and electrons were set to match those of the beamline for different runs: namely, momenta of 5, 10, 20, and 30 GeV/c. The medium and algorithm parameters for the different radiators had to be changed for separate runs.

5.3.1 Modeling of Ionisation Energy Loss

Before discussing the models of ionisation energy loss offered by GEANT it is necessary to first introduce a few basic parameters that are critical for the optimisation of these routines. Foremost among these are the energy cuts, that is, the energy below which GEANT ceases to track each particle type. When the particle's energy drops below this minimum the remaining energy of the particle is deposited at the location in the detector where tracking ceases. The optimal energy cuts for the various particle types must be determined by the user and those used for the TRD simulation will be justified shortly.

Another important parameter requiring optimisation is the threshold above which δ-rays are explicitly generated. Here it is important to distinguish the energy *lost* by an incident particle from the energy *deposited* by that particle in the medium of interest. The theoretical Landau distribution, for example, concerns itself with the energy lost by charged particles as they traverse a given thickness of matter. Recalling that this energy loss consists of ionisation of the atoms in the medium, it is immediately obvious that the ionised δ-rays will be free to wander through the medium and thus will have a certain likelihood of escaping the volume in which they were produced. In this case a fraction of the energy lost by the incident particle in a medium will in fact not be deposited in that medium. This effect will occur, for example, in the detector gas, where a small fraction of the energy loss will not be deposited in the wire cell of interest, namely the one traversed by the primary particle track.

Of more significant impact, δ-rays produced in the comparatively dense material of the radiator may penetrate, or 'punch-through', into the X-ray detector, depositing a portion or all of their energy there. Although the δ-rays tend to be ejected at a large angle to the incident track, as mentioned previously through multiple scattering their direction is quickly randomised. Thus in the case of a multi-module TRD this randomisation implies that the punch-through effect may affect the *preceding* X-ray detector as well as the following one. Very high energy δ-rays, which are more strongly forward peaked, may even cross several detector modules. For pion events punch-through δ-rays will have a significant impact on the rejection power of the TRD,

noting that the occasional punch-through radiator δ-ray will have a large influence on the small statistics of the high energy tail of the pion distribution.

In light of the above, accurate tracking of δ-rays is seen to be critical to reproduce the distribution of energy *deposited* in the detector. Thus GEANT's unofficial claim to provide accurate particle tracking and energy loss down to 1 keV is seen to be an attractive feature not only for X-ray photoabsorption, but also for the tracking of δ-ray electrons.

In order to accommodate the above distinction between energy loss and energy deposition, in GEANT the calculation of energy loss fluctuations can be limited by some maximum energy transfer. This maximum energy transfer is determined by the δ-ray generation threshold mentioned previously and a model distribution of 'restricted' fluctuations is sampled below this threshold and δ-rays are generated explicitly above it. In thin layers GEANT offers two different models of energy loss which support this option, namely the Urban model and the photoabsorption ionisation (PAI) model.

The PAI model is a new feature of GEANT added into the package specifically for modeling of ionisation energy loss in very thin layers [26, 28]. The method uses photoelectric cross sections to describe the detailed nature of atomic structure in order to better estimate the fluctuations in energy transfer for the small number of individual collisions which characterise thin layers. A similar photoabsorption method was used in the original hybrid TRD simulation to determine the energy loss fluctuations and this similar method was found to be satisfactory.

The Urban model on the other hand is GEANT's older default method for explicit generation of δ-rays above a given threshold. This simple model is advertised as valid for any detector thickness. The model parameterises the atoms of the medium with two excitation energy levels and one ionisation cross section to reproduce both the low and high energy transfer collisions [26].

In order to test these models of energy loss the results of simulation were compared primarily to the pion distributions of energy loss measured in the prototype TRD test experiment. Comparison with the pion distributions allows for tests focusing on the ionisation energy loss and δ-ray tracking, noting that for pions the further

complexity of low energy X-ray transition radiation generation and absorption is absent. Experimental ionisation distributions for electrons, obtained in the case of no radiator in front of the X-ray detector, were also used for comparison. However, the electron distributions could not include the important effect of punch-through δ-rays from the radiator and thus were not as critical as a standard of comparison as the pion distributions.

As mentioned earlier, optimal δ-ray tracking is essential since δ-rays either penetrating or escaping the relevant wire cell volume have a large influence on the small statistics of the high energy tail of the energy deposition distribution. In turn, it is specifically the integral of this tail above the electron efficiency cut which determines the pion rejection factor of the TRD. Therefore, in light of GEANT's unofficial claim of reliable δ-ray generation and tracking down to 1 keV, these models were tested with 1, 5, and 10 keV cuts on both electron tracking and δ-ray production. For the PAI model the results displayed alarming sensitivity to the different cuts and with 1 and 5 keV cuts the comparison with data was poor. With 10 keV cuts the simulation results for the PAI model converge to good agreement with the data. The results of the comparison to data for the PAI model with 5 keV cuts are shown in fig. 5.1 and with 10 keV cuts in fig. 5.2. The GEANT developers were contacted regarding this alarming sensitivity to cuts below 10 keV and eventually identified the origin of the PAI model failure. Apparently the unfulfilled assumption of the model for cuts below 10 keV is that the δ-ray threshold must be much greater than the ionisation potential, I, of the gas, and this assumption failed for cuts below 5 keV or so for xenon for which I is of order 0.5 keV [28].

The Urban model results on the other hand were self-consistent with cuts down to 1 keV. The results with 5 keV cuts are given in fig. 5.3 and with 10 keV cuts are given in fig. 5.4. The agreement with the data is seen to be good in both cases.

In light of the sensitivity of at least one of the models to low energy cuts on δ-ray generation and out of consideration for the finite CPU time available for tracking low energy particles, the δ-ray generation and tracking threshold required for accurate TRD simulation was evaluated more carefully. The dominant factor determining the maximum acceptable cut is the range of the δ-ray electrons. The effective range of

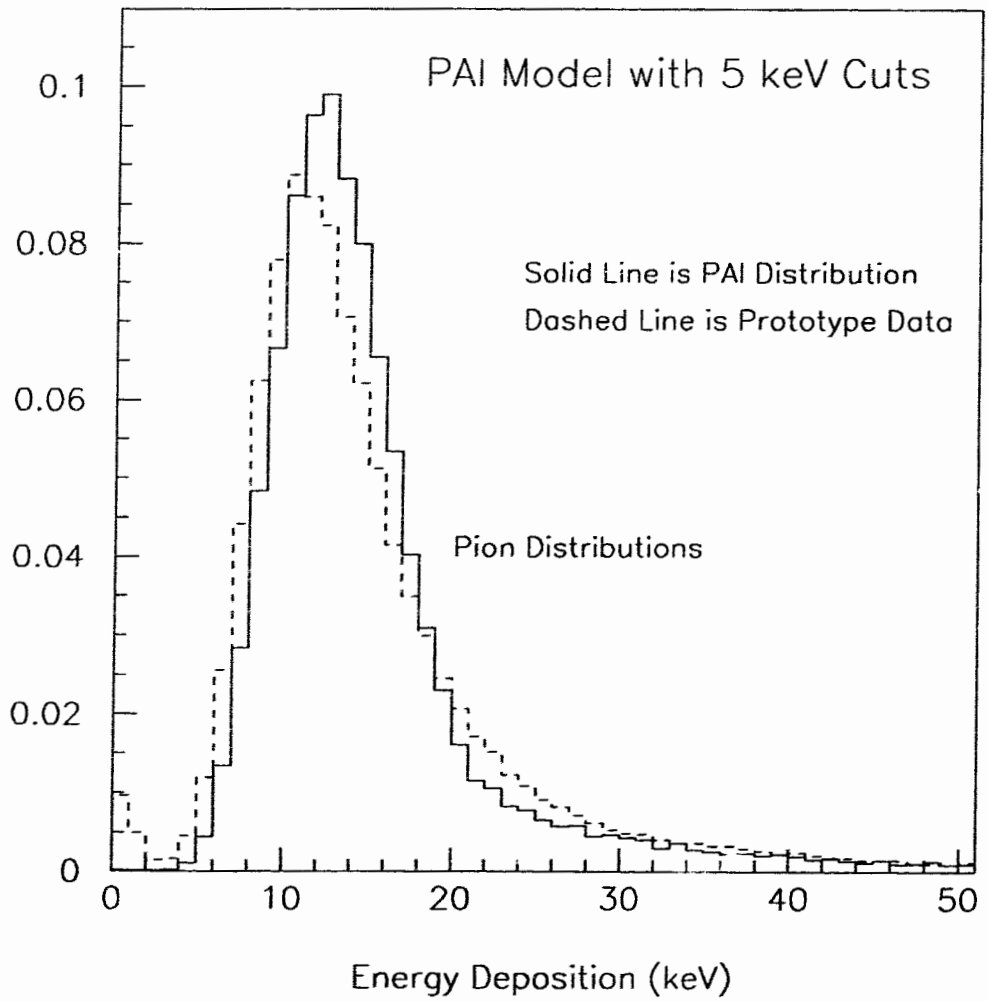

Figure 5.1: The PAI model for ionisation energy loss with 5 keV cuts compared to the experimental pion distribution.

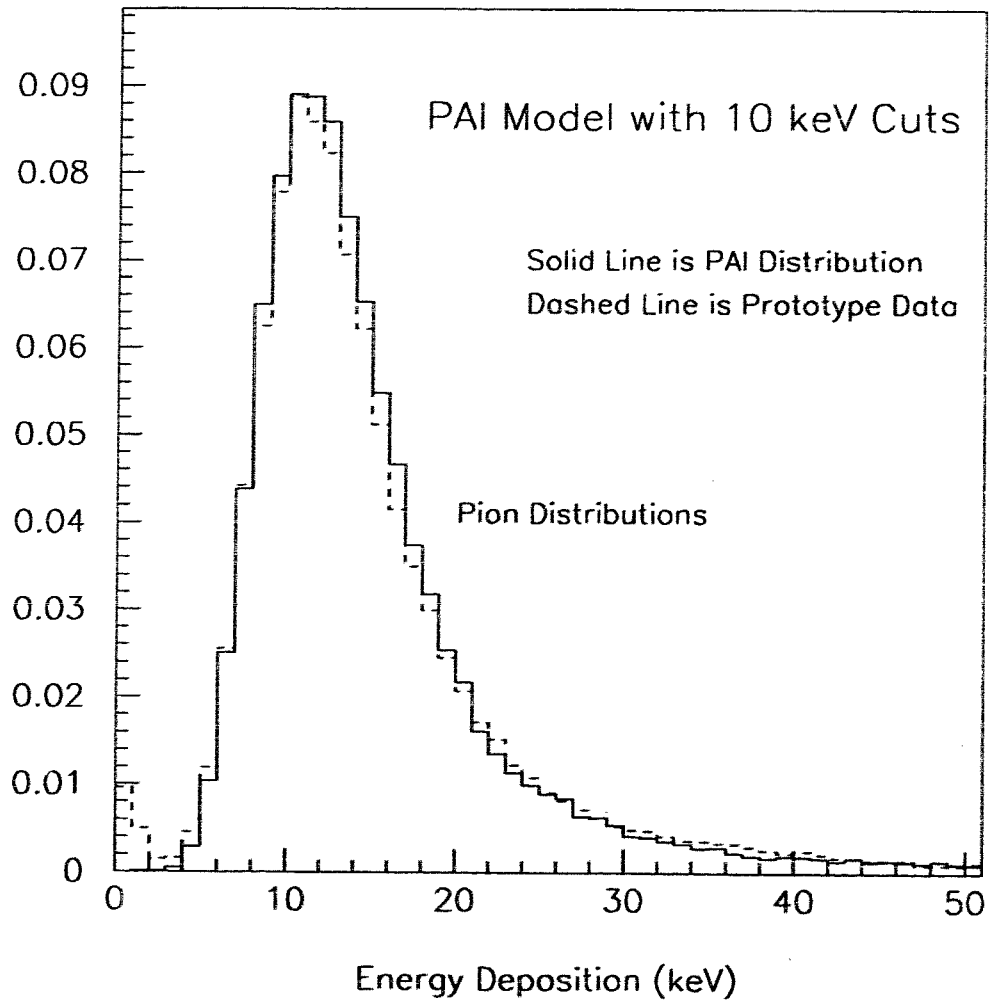

Figure 5.2: The PAI model for ionisation energy loss with 10 keV cuts compared to the experimental pion distribution.

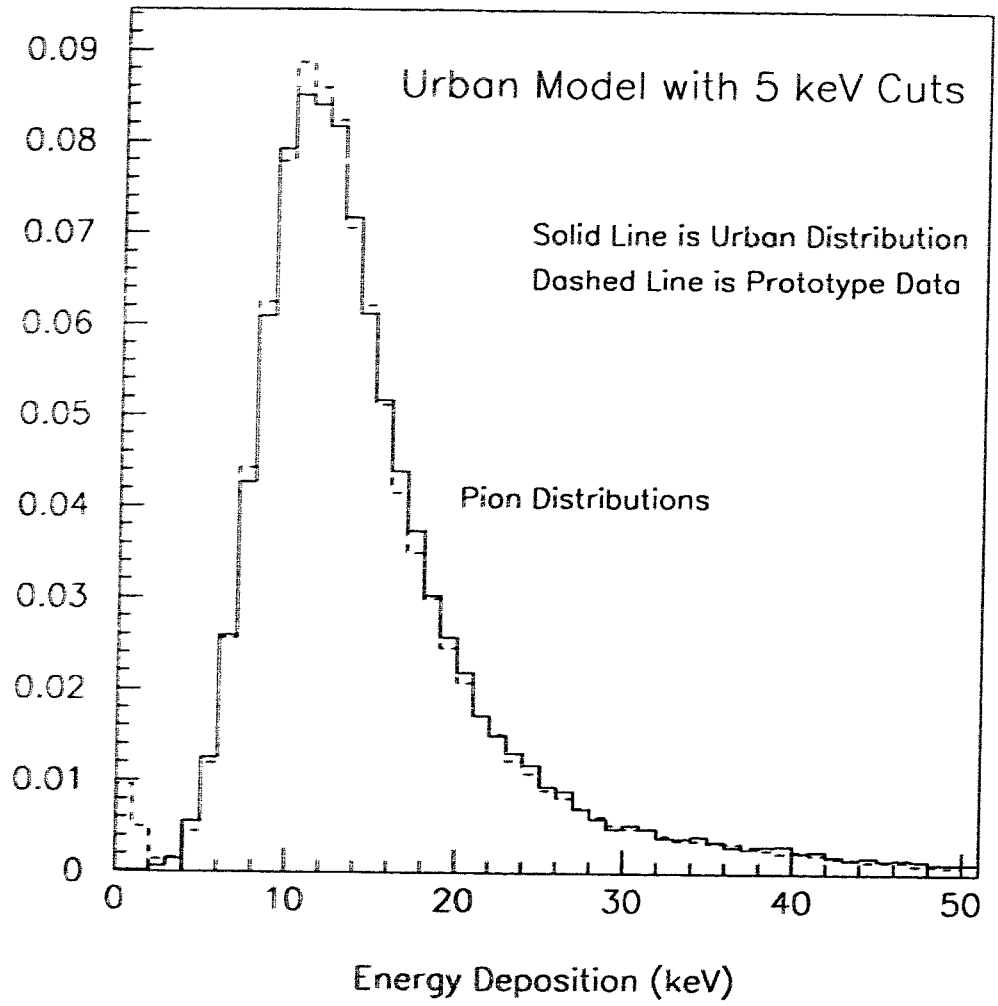

Figure 5.3: The Urban model for ionisation energy loss with 5 keV cuts compared to the experimental pion distribution.

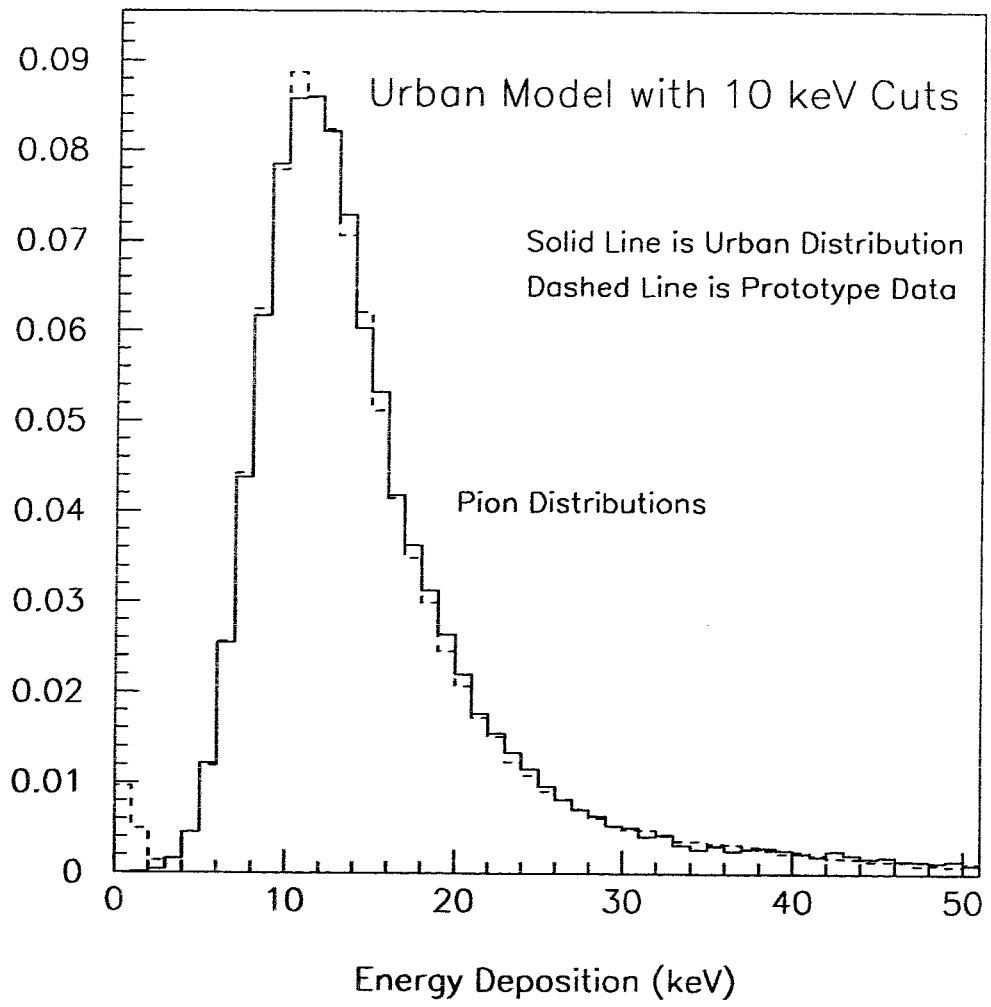

Figure 5.4: The Urban model for ionisation energy loss with 10 keV cuts compared to the experimental pion distribution.

δ-ray electrons can be approximated up to a few hundred keV by [25],

$$R = 0.71E^{1.72}, \tag{5.11}$$

where R is in g/cm^2 and E is in MeV. Using this formula, a more moderate electron energy cut of 10 keV implies a maximum effective range for the *untracked* δ-rays of order only 0.5 mm in the Xe/CH_4 gas mixture. This is less than 2% of the active area of 1 wire cell in the prototype TRD and less than 4% of the active area of 1 wire cell in the HERMES TRD.

Since under actual experimental conditions the TRD tracking alignment accuracy in the HERMES experiment will likely not exceed 1 mm, this energy cut on δ-ray tracking in the gas would be within the track reconstruction tolerance, noting that it is the track reconstruction which identifies which TRD wire cells are to be associated with a given track. Moreover, δ-rays emitted from the radiator would have a similar maximum range in the flush gap, that is, any δ-rays with energy below 10 keV would be unlikely to reach the detector gas, and thus the 10 keV threshold is adequate also in consideration of the punch-through δ-rays.

In light of these calculations the agreement of TRD prototype data with simulation results with a 10 keV energy cut on electron tracking is not unexpected. Further, the above considerations also imply that 10 keV electron cuts would be adequate for simulation of the HERMES TRD. Although both models agreed with the data with 10 keV δ-ray generation and electron tracking cuts, due to superior agreement in the critical high energy tail of the pion distribution and also a faster algorithm, the Urban model was chosen over the PAI model.

5.3.2 Modeling of Transition Radiation

A model for the generation of transition radiation is unfortunately not available within the GEANT package. The independent TR generator which was explicitly included in the TRD simulation was the one of the earlier hybrid TRD simulation, which had been developed starting from elements of a generator obtained from the D0 collaboration [29]. This TR generator is based on a numerical method of Garibian *et al.* [30] which evaluates the TR yield from an irregular stack of dielectric layers.

Defining $< dN_p/d\omega >$ to be the average number of TR photons per unit frequency emitted by a stack of N layers of average thickness $< a >$ and average spacing $< b >$, and θ to be the angle of emission of the transition radiation, then,

$$\left\langle \frac{dN_p}{d\omega} \right\rangle = \int \left\langle \frac{d^2N_p}{d\omega d\theta} \right\rangle d\theta, \tag{5.12}$$

where,

$$\frac{d^2N_p}{d\omega d\theta} = \frac{2\alpha\theta^3}{\pi\omega} \left[\frac{1}{1-\beta^2\epsilon+\theta^2} - \frac{1}{1-\beta^2+\theta^2} \right]^2 I. \tag{5.13}$$

Here I is a general interference term which is a rather complex function of a, b, θ, β, and $\epsilon = 1-\xi^2$. The reader is referred to the original article [30] for the full expression.

If the distribution for the thicknesses and spacings of the layers is given by a function, $f(x)$, then the averaging of eq. 5.12 can be performed as follows,

$$\langle \ldots \rangle = \int_0^\infty \ldots f(x)dx, \tag{5.14}$$

assuming that the integral of the function $f(x)$ is normalised to unity.

Garibian et al. [30] approximate the distribution $f(x)$ with a gamma distribution,

$$f(x) = \frac{\beta_0^\alpha x^{\alpha-1} \exp(-\beta_0 x)}{\Gamma(\alpha)}, \tag{5.15}$$

where $\Gamma(\alpha)$ is the Euler gamma function, and α and β_0 are real positive non-zero parameters determined from:

$$\begin{aligned} \alpha/\beta_0 &= \langle x \rangle, \\ \alpha/\beta_0^2 &= \langle \Delta x^2 \rangle. \end{aligned} \tag{5.16}$$

where $\langle x \rangle$ and $\langle \Delta x^2 \rangle$ are the average value and mean square deviation of the dielectric layer thickness. Thus α determines the variation through:

$$\sqrt{\frac{1}{\alpha}} = \frac{\sqrt{\langle \Delta x^2 \rangle}}{\langle x \rangle}. \tag{5.17}$$

The gamma distribution allows for the averaging in eq. 5.12 to be performed analytically. The integration over angles in eq. 5.12, however, must be evaluated numerically.

In the absence of experimental results for TR X-ray generation alone, that is to say, *disentangled* from both the effective amount of TR absorbed in the detector gas and from the underlying ionisation of the electron track, the performance of the TR generator can only be compared to experimental data in terms of the total electron distribution. This comparison will be made after consideration of the modeling of photoabsorption.

5.3.3 Modeling of Photoabsorption

Photoabsorption in GEANT is calculated using parameterisations of the known photoabsorption cross sections for all the elements, as a function of photon energy E_γ, where the mass attenuation coefficient of eq. 5.10 is fit as follows (for $Z \leq 100$),

$$\mu_{ij} = \frac{C_{1,ij}}{E_\gamma} + \frac{C_{2,ij}}{{E_\gamma}^2} + \frac{C_{3,ij}}{{E_\gamma}^3} + \frac{C_{4,ij}}{{E_\gamma}^4}. \tag{5.18}$$

Here the index i runs over elements and j over the number of fitting intervals; μ is in cm^2/g. As mentioned above, GEANT had recently unofficially extended the parameterised photoabsorption cross sections down to 1 keV. It is this new feature which made GEANT attractive for accurately simulating the critical photoabsorption in the soft X-ray energy range above a few keV.

GEANT also tabulates four shell energy levels for each element, namely K, L_I, L_{II}, L_{III}, as well as their radiative and non-radiative decay mode probabilities. This allows GEANT to include the effects of both fluorescence and radiationless transitions subsequent to the photoelectric absorption [26].

5.4 Comparison to Experimental Data

In light of the above considerations, the Urban model was chosen for simulation of ionisation energy loss fluctuations with explicit δ-ray generation above 10 keV and electron tracking down to 10 keV. For the TR generator, the parameter $\alpha^{-1/2}$ of eq. 5.17 was set to 0.1 and 1.0 for the variation of the cylindrical fibre thicknesses and spacings respectively. These best fits were determined in the previous 'hybrid'

simulation [29]. The photon tracking cut was set at 1 keV. The final simulation results with these optimised cuts are compared in fig. 5.5 to the experimental pion and electron distributions at 5 GeV obtained with the 17–20 μ fibre radiator. The simulated and real data can be seen to agree well over the full range of interest.

The simulation performance is also compared to test data at 10 GeV in fig. 5.6. As can be seen from the figure the simulation results at higher energy also agree well with the data. In particular, the upward shift of the pion spectrum with increasing beam energy reflects the relativistic rise of ionisation energy loss mentioned previously. The comparative insensitivity of the electron spectrum to incident beam energy reflects both the saturation of the relativistic rise of energy loss as well as the saturation of TR generation. These topics will be addressed in greater detail in the following section.

The above studies indicate that with optimised cuts and parameter settings, as well as propitious choice of energy loss model, GEANT is capable of accurately reproducing the relevant ionisation energy loss fluctuations necessary for simulation of the TRD. Further, the algorithm for TR generation and the GEANT photoabsorption are also successful at reproducing the TR X-ray generation in the irregular fibres of the radiator and absorption in the radiator itself as well as in the detector gas.

Following this success two efforts were undertaken. The first of these was to include the TR generator, the relevant TRD simulation routines, and the optimised GEANT parameter settings into the HERMES Monte Carlo simulation. The second was to convert the simulation of the prototype TRD into a simulation of the full six module HERMES TRD. The motivation for and use of this simulation of the six module HERMES TRD are the subjects of the following section.

5.5 Study of HERMES TRD Response Distributions

In the case of the prototype TRD test experiment and also in the case of Monte Carlo simulation, the incident particle type is known *a priori*. This information allows for the determination of the statistical distributions of energy deposition for each particle

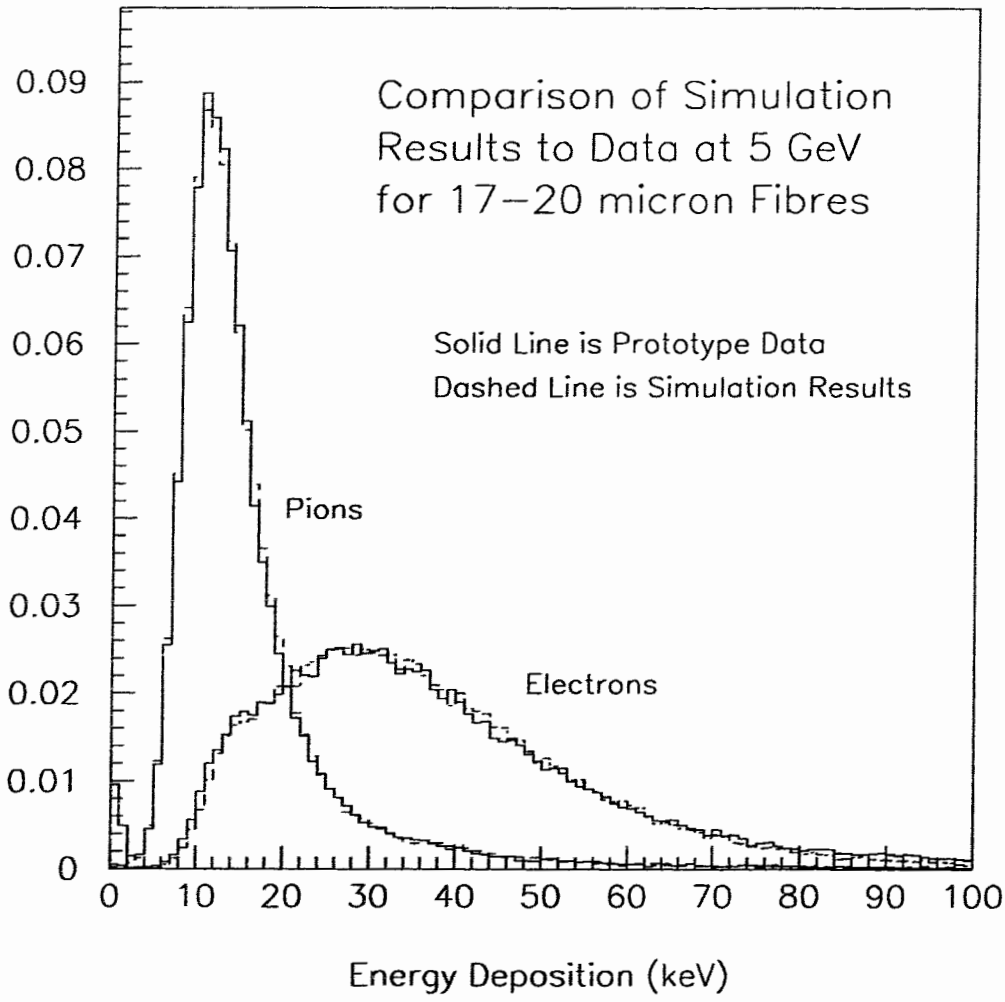

Figure 5.5: The simulation results for 17–20 μ radiator compared to the 5 GeV electron and pion distributions obtained from TRD prototype data.

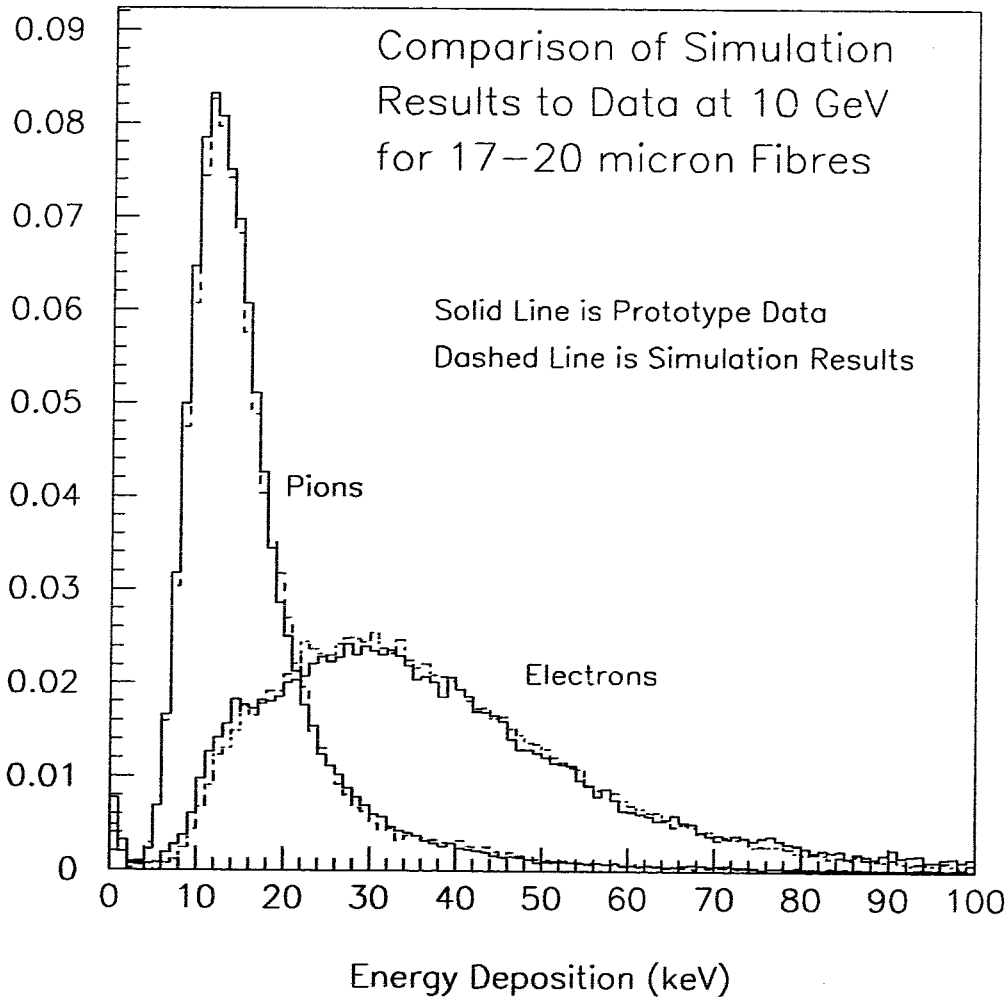

Figure 5.6: The simulation results for 17–20 μ radiator compared to the 10 GeV electron and pion distributions obtained from TRD prototype data.

type. Under actual experimental conditions the particle type is not known *a priori* and the task of the PID algorithms is to identify the incident particle type given the specific detector responses to that event and using the *known* detector response distributions.

Since the spectra for pions and positrons are known to overlap significantly, as was shown for example in fig. 3.1, the probability that an event can be identified with a given particle type becomes a function of the *height* of the known response distribution for that particle at the value of energy deposition measured in each detector. Thus knowledge of these response distributions for all particle types and for each detector (or module) is essential to the PID analysis.

A further point of complexity is introduced however in recognition of the fact that the energy deposition distributions for both pions and positrons, indeed for all particle type candidates, are dependent upon the incident track angle and momentum as well as a number of other conditions which will be outlined below. Thus, in order to optimise the particle identification algorithm, the response distributions must be determined for all combinations of the known conditions which define the event.

Though in principle these studies could be performed with the HERMES Monte Carlo simulation, for flexibility as well as speed considerations the prototype TRD simulation was simply upgraded to a simulation of the six module HERMES TRD with some background effects from the spectrometer environment included. The most significant sources of correlated background from the HERMES spectrometer were anticipated to be the upstream scintillator material, which induces hadronic secondaries, and the lead sheet of the preshower, which introduces backscattered background particles into the TRD acceptance. To accommodate these effects the above materials were included in the geometry definition. Events were then accumulated under the range of possible kinematic conditions to study the anticipated kinematic and detector dependent variations in the TRD response distributions.

The relevant kinematic information available for the TRD analysis after each event is the momentum, angle through the TRD, and charge of each track. These parameters are determined from the position measurements of the tracking chambers coupled with the track deflection through the magnet. Before presenting the simulation results on

the variation of the response distributions under the different kinematic conditions, it will be instructive to briefly review the physical origin of each variation.

5.5.1 Momentum Dependence of Response Distributions

Considering first the transition radiation, the variation of the TR generation is limited by the γ dependent saturation effect which was given by eq. 3.7. This saturation of the yield resulted from the non-zero plasma frequency of air and, using eq. 3.7, this saturation value can be estimated. Noting that $\omega_P^{air} = 0.7eV$, for 10 keV X-rays a γ value of roughly 10^4 can be anticipated for the onset of saturation of the yield. This corresponds to 5 GeV positrons. Thus over the momentum range of interest the TR yield is beginning to saturate and will increase only slightly.

In terms of ionisation energy loss, as shown in eq. 5.1, the average dE/dx for charged particles is known to begin to increase after some mass-dependent threshold. The energy loss preceding this relativistic rise is called minimum ionising and the saturation following this rise is called the Fermi Plateau. Around the lower momentum limit of 3.5 GeV/c for events of interest in the HERMES experiment, pions are only about half way up the relativistic rise curve. On the other hand positrons are already ionising at the saturation value of the Fermi plateau.

The above considerations imply that the average value of the energy deposition spectra for both pions and positrons should migrate upwards slightly with increasing track momentum. This behaviour is confirmed in fig. 5.7 which shows the response distributions for pions and positrons at 4 and 28 GeV/c.

5.5.2 Angular Dependence of Response Distributions

Considering next the angular dependence, the variation of TR generation and self-absorption in the radiator can be expected to be negligible. This follows from the fact that the total number of cylindrical fibres traversed by the incident track will be independent of the incident angle, as will the net amount of fibre material (absorption in air being negligible in comparison to fibre material).

The TR absorption in the *detector*, on the other hand, will increase slightly at

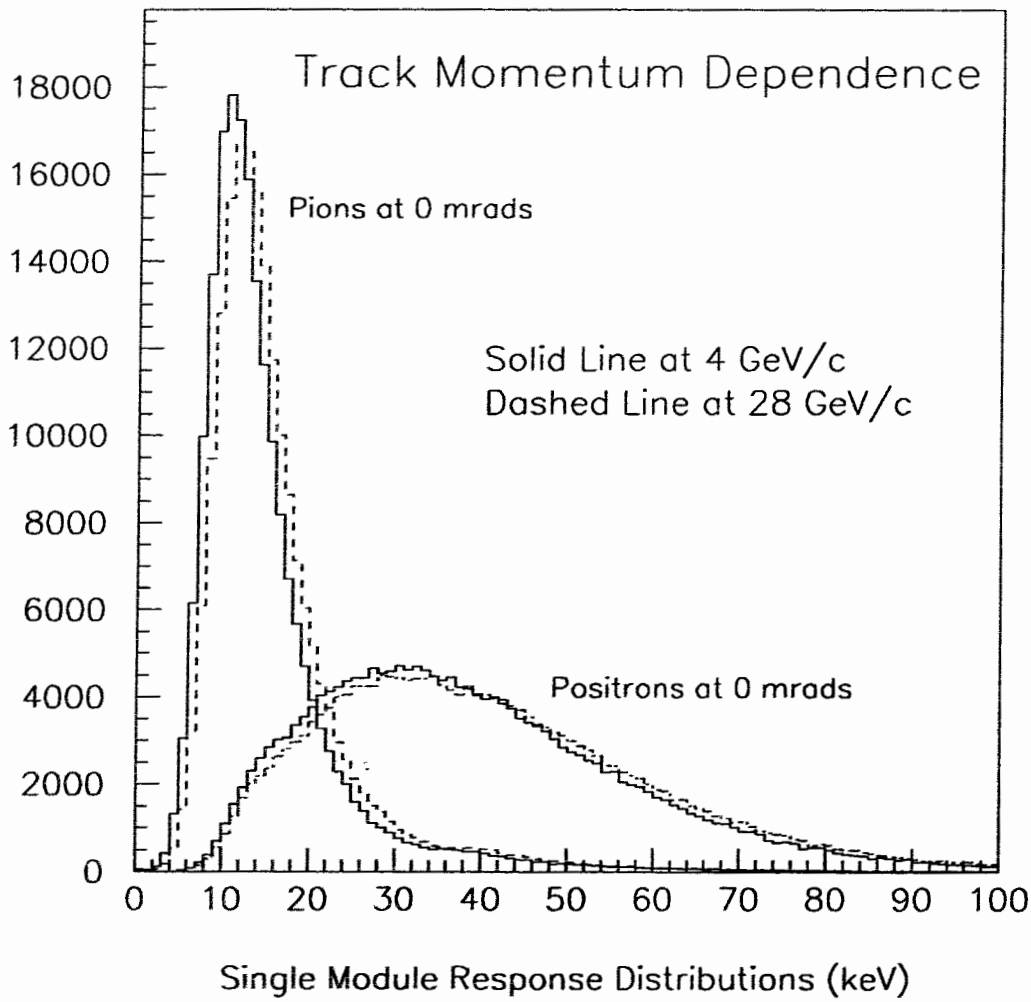

Figure 5.7: The energy deposition distributions for 4 and 28 GeV/c incident tracks in module 3 as determined by Monte Carlo simulation.

large angles since the net amount of gas traversed will increase as $\cos^{-1}\theta$, which is at most a 3% increase in length at maximum track angle. It is important to note, however, that the additional absorption does not vary linearly with this geometrical factor since the attenuation of radiation is an exponentially decreasing function, as given by eq. 5.10 earlier.

In terms of ionisation energy loss, as given by eq. 5.1, the average dE/dx is proportional to the thickness of the medium. The increase of the detector length by the factor $\cos^{-1}\theta$ implies an increase of roughly 3% in the average dE/dx for a maximum track angle of approximately 15 degrees. This corresponds to a shift in the spectrum of only 0.33 keV.

These effects are shown in fig. 5.8 which compares the pion and positron distributions at 0 and 250 mrads. The angular dependence is seen to be slightly less significant than the momentum dependence.

5.5.3 Simulation Results for Detector Effects

In addition to the kinematic effects presented above there are also background and detector effects which influence the energy deposition distributions. The figures shown above were response distributions given by the 3rd module of the TRD. In fact, although the module dependence of the distributions was *anticipated* to reflect the increasing impact of hadronic showers and of the contribution from backscattering from the lead sheet in downstream modules, another import effect was discovered. In particular, the positron energy deposition was observed to increase with increasing module number. This effect, which improves the particle discrimination of the later modules, arises from 'punch-through' transition radiation produced in an upstream radiator but only absorbed in the second or even third subsequent X-ray detector. In fig. 5.9 the distributions for modules 1 and 6 are presented. The impact of this punch-through TR effect is seen to be significant.

Finally, all of the figures shown have been generated under the condition that the particle track is completely contained within a single wire cell. In general, with

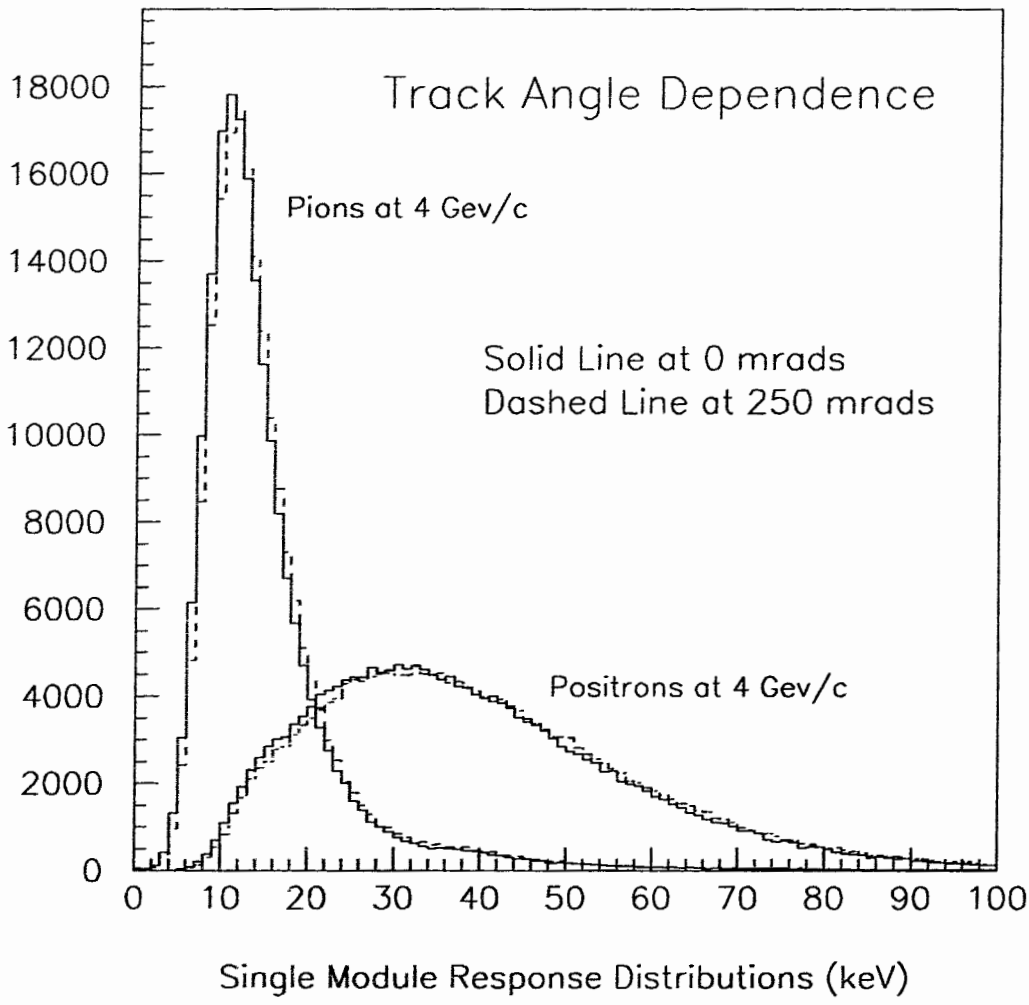

Figure 5.8: The energy deposition distributions for 0 and 250 mrad track angles in module 3 as determined from Monte Carlo simulation.

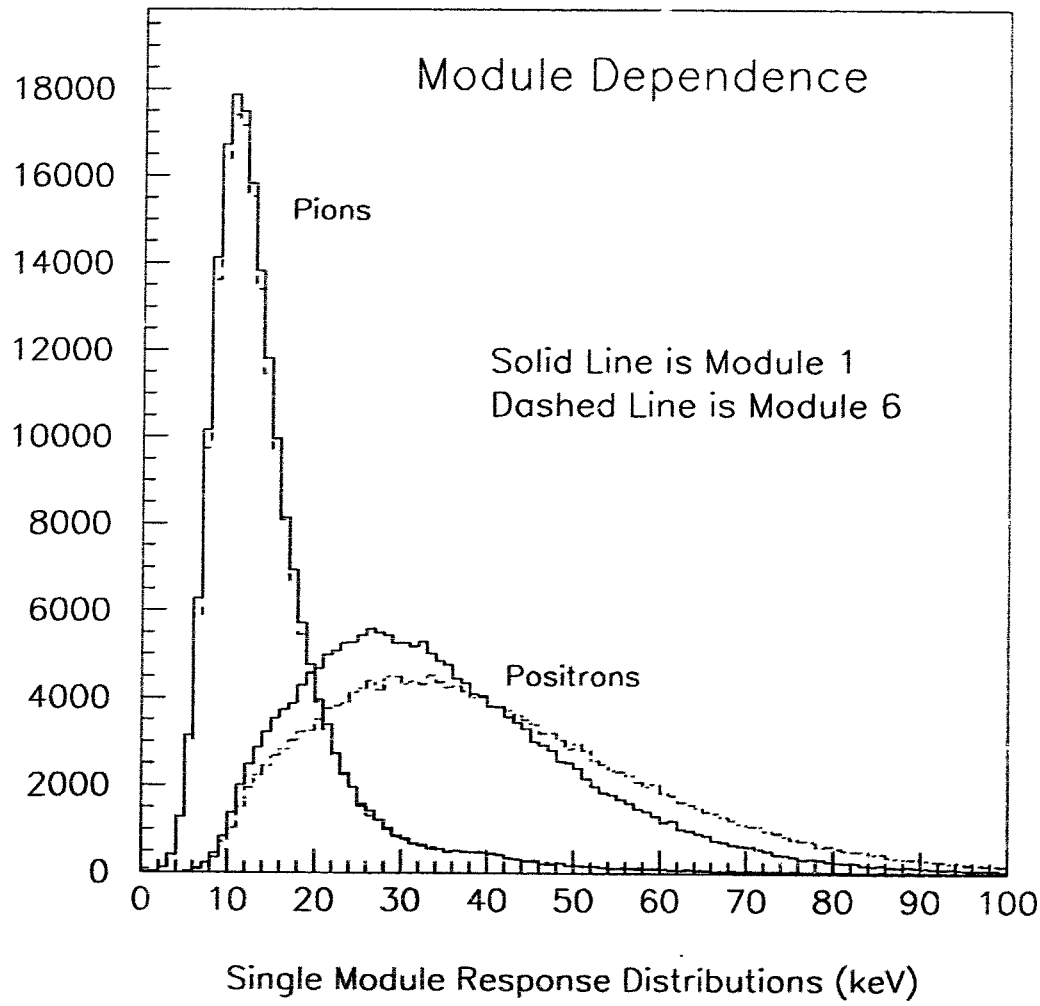

Figure 5.9: The energy deposition distributions in TRD module numbers 1 and 6 at 4 GeV/c for positrons and pions as determined by Monte Carlo simulation.

increasing track angle there is an increasing likelihood that a particle track will traverse two adjacent wire cells in the same module. Further, even a straight track may straddle the median between two adjacent wires. Under these conditions the TR absorption (if any) will be distributed in both wire cells requiring the summation of these two wire cells to obtain the full signal. The relative frequency of events where 2 wires must be summed for the total energy deposition is a complex function of the track angle , tracking alignment accuracy, and the *a priori* distribution of tracks incident upon the TRD according to the deep inelastic and photoproduction scattering processes.

In fig. 5.10 the distributions for pions and electrons are compared for the cases when the track crosses one or two wire cells in a single module. Though visually the impact may appear small, it is important to recall that the sensitivity of the pion rejection factor to the increased background which occurs when two adjacent cells must be included in the sum for a single module is significant because of the impact this extra background will have on the small statistics of the high energy tail of the pion distribution. To emphasize this point the six module truncated mean spectra for 1 wire and 2 wires in the energy deposition sum of each module are compared in fig. 5.11. The effect on the high energy tail of the pion distribution is now obvious. As mentioned previously, the dominant contributions to this background are hadronic 'showers' and punch-through δ-rays. Further, the above sensitivity to the wire sum is a minimum estimate based only on those sources of background explicitly included in the simulation, namely correlated background from the upstream scintillator material and the lead sheet following the TRD.

5.5.4 Monte Carlo Generation of Response Distributions

In light of the above studies, the response distributions required for the PID algorithm were generated for three values of both track angle and momentum, leading to a total of nine permutations in momentum and angle. This allows for a quadratic fit in both momentum and angle for any given event. The values of momentum were 4, 10 , and 28 GeV/c and the values of angle were 0, 100, and 250 mrads. Further, each

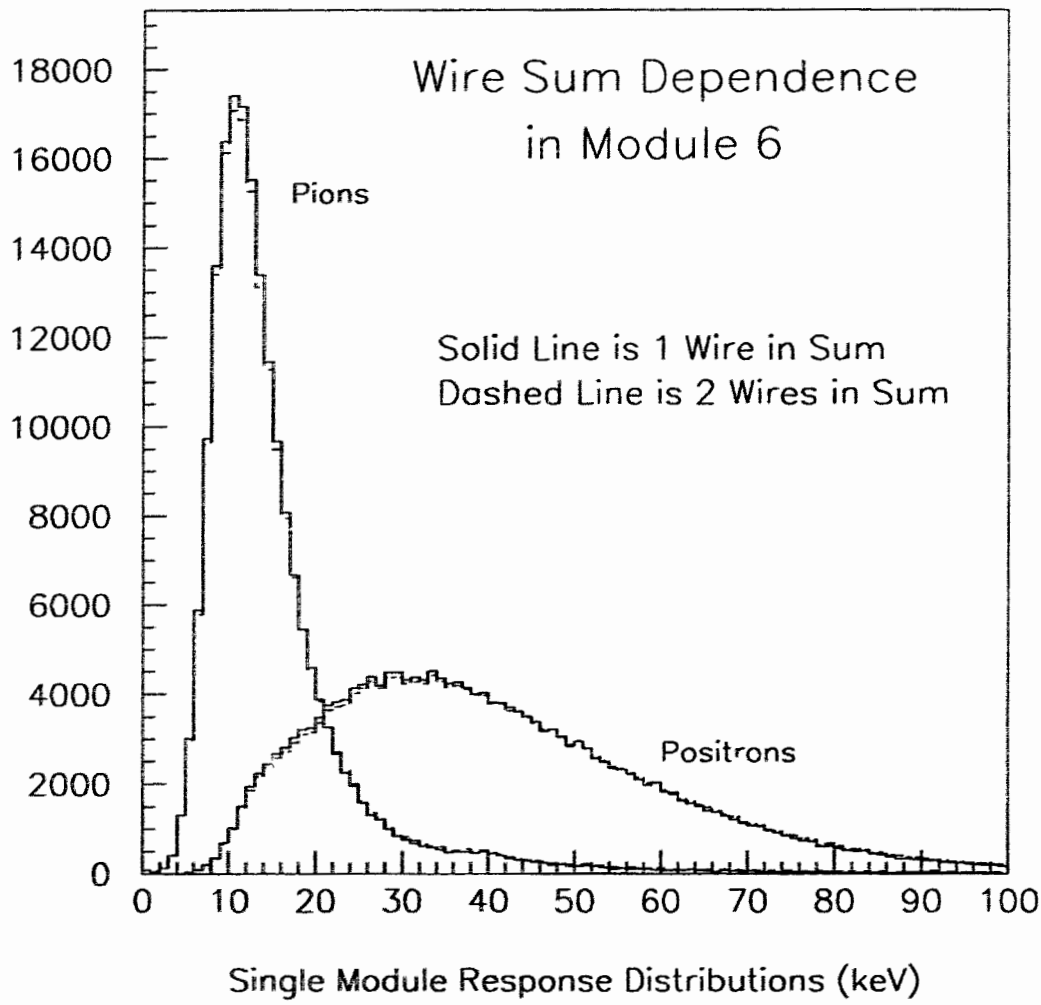

Figure 5.10: The energy deposition distributions for 1 and 2 wires included in the energy deposition sum for pions and positrons in module 6 as determined by Monte Carlo simulation.

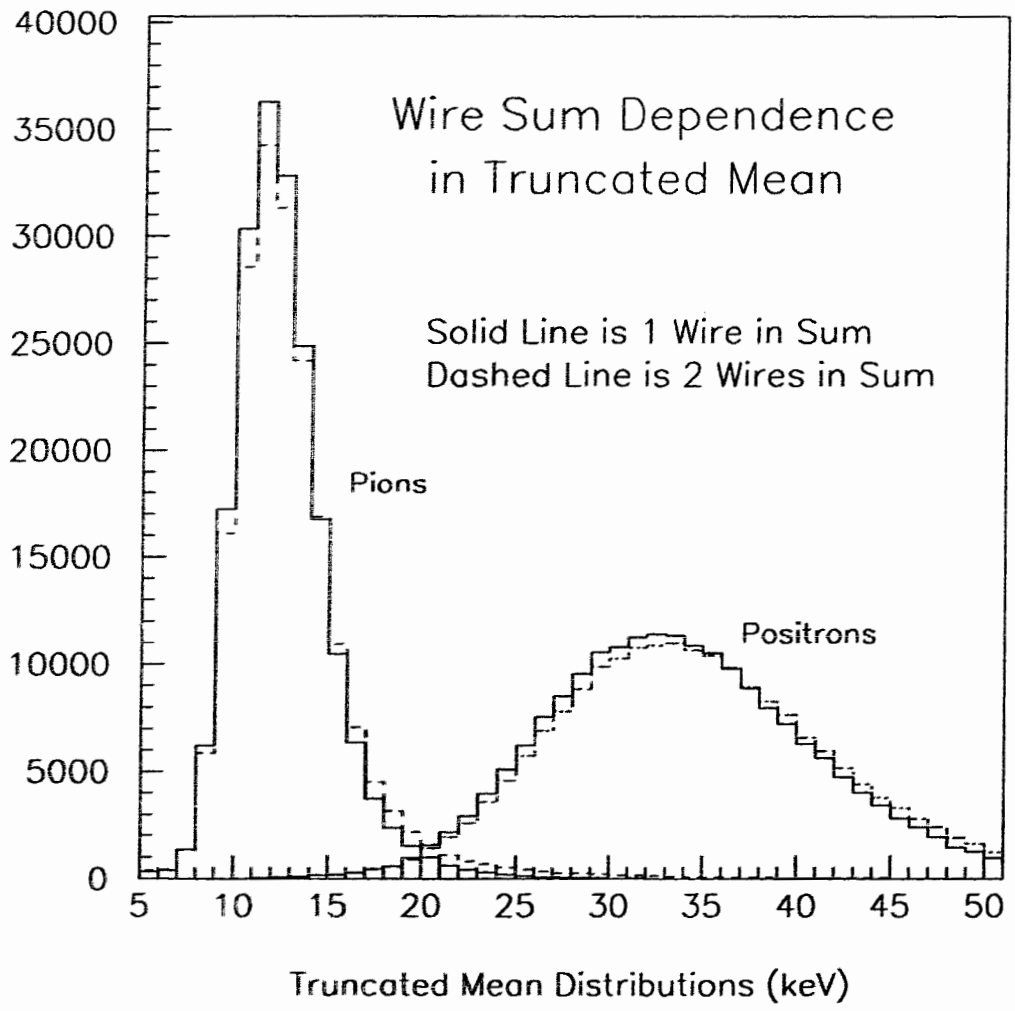

Figure 5.11: The energy deposition distributions in the six module truncated mean for 1 and 2 wires in the energy deposition sum.

permutation of momentum and angle was generated for both wire sum possibilities; for the case in which the track was completely contained within one wire cell and for the case in which the track crossed two wire cells.

Thus with 3 momentum and 3 angle values, 6 modules, 2 wire summing possibilities, and 2 primary particle types, the total number of distributions available for interpretation of the TRD data is 216. Each distribution extended from 0 to 100 keV with a bin size of 1 keV and was generated with 5×10^5 events. The details of the algorithms which use these distributions for the TRD PID and the proposed HERMES PID algorithms are presented in the following chapter.

Chapter 6

Particle Identification Analysis

The task of the particle identification (PID) algorithm is to convert the energy deposition signals recorded in the detectors for a given event into a quantitative measure of particle type. In particular, for the six modules of the transition radiation detector (TRD), the results of all modules for a given track must be combined in an optimal manner to obtain a complete TRD measurement of the particle type. The probabilities obtained from the other PID detectors must then also be combined with the TRD measurement in a consistent way to make the final experimental determination of the particle's identity.

In this chapter the method of interpretation of the TRD measurements is first introduced qualitatively. This will be followed by a review of relevant concepts from probability theory which will be applied first in an algorithm for the TRD PID and then in a final algorithm for combining the results of all PID detectors.

6.1 Overview of Probability Method

The performance of the prototype TRD was extrapolated to the six module TRD performance using the truncated mean method. However, optimal interpretation of the TRD results involves a probability analysis which uses the information from all TRD modules. Therefore the Monte Carlo studies of the previous chapter were based on individual module rather than truncated mean distributions. For each module's

response then a probability can be extracted from each module's predetermined energy deposition distributions for each particle type candidate.

The response distributions have all been generated under an equal ratio of pions to positrons. Under actual experimental conditions, however, the relative flux rates of pions, kaons, protons, and positrons are neither equal nor constant with varying momentum and scattering angle. Thus a straightforward extraction of the relative heights of each particle type's distribution at the given value of energy deposition is not a valid basis for comparison. In fact the relative flux rates of the different particle types must be included to normalise, or weight, the energy deposition distributions as a function of incident angle and momentum.

The importance of these factors in the PID formulae can be understood more qualitatively with the aid of a simple example. Consider the extreme case where under certain experimental conditions, say at a certain momentum and angle, the production of positrons is zero. Then use of the response distributions without weighting for extracting probabilities would occasionally yield a 'maximum' probability that the incident particle was a positron when in fact the true probability is zero. Under less extreme and more realistic circumstances, the incident flux information is at the very least an important weighting factor in the determination and comparison of particle type probabilities.

A visual example of the above argument is presented in fig. 6.1, where the single module pion distribution has been scaled by a factor of 40. This factor is the anticipated flux ratio of pions to positrons (at 4–5 GeV and intermediate angles) once the events have been filtered by the first level trigger. From this figure it is clear that a simple comparison of the heights of the response distributions which are normalised to equal numbers of events for each particle type is not a valid basis for ascertaining probabilities. Fig. 6.2 is also provided as an example of the impact of the scaling on the truncated mean spectra. These truncated mean distributions provide a comparative measure of the increased net pion contamination when incident flux rates are taken into account. The quantitative method of analysis developed for combining and interpreting probabilities which accommodates this flux dependence is introduced in the following section.

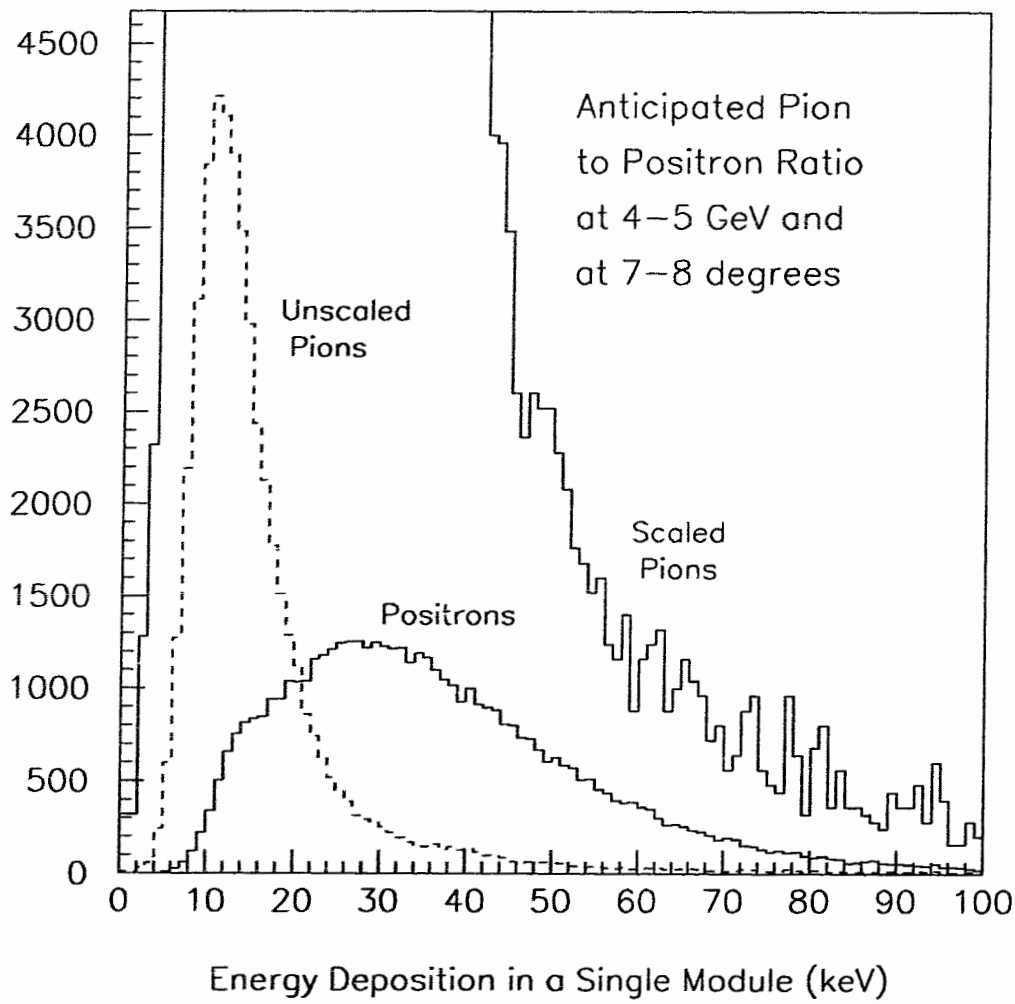

Figure 6.1: The relative scale of pion to positron distributions estimated from the anticipated incident flux ratio.

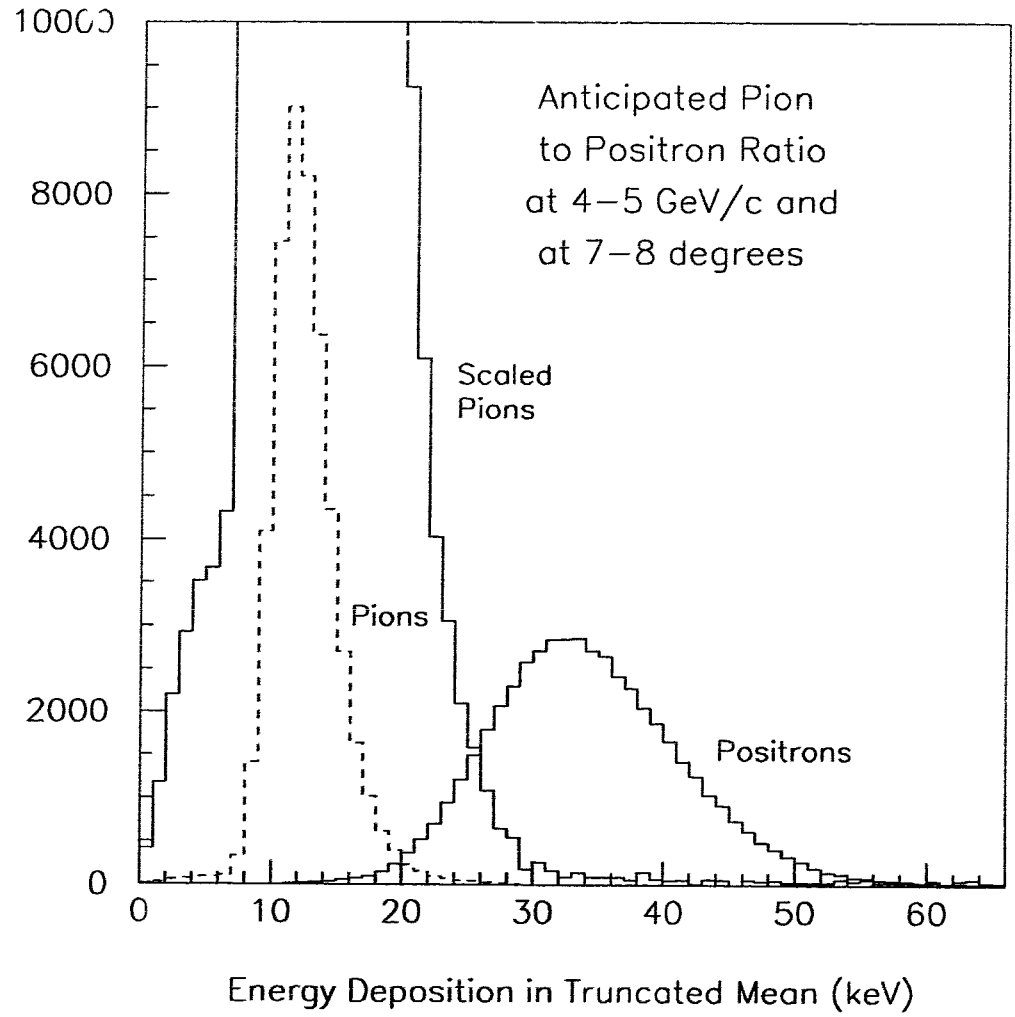

Figure 6.2: The relative scale of pion to positron truncated mean distributions estimated from the anticipated incident flux ratio.

6.2 Maximum Likelihood and Bayes Theorem

Let $f_i^m(E)$ be the known distribution of energy deposition E for particle type i in module m under the kinematic and detector conditions which define the incident track and let E_m be the specific energy deposition in module m from this track. If the integral of this distribution is normalised to unity,

$$\int_0^{E_{max}} f_m^i(E)dE = 1, \tag{6.1}$$

where E_{max} is the greatest relevant value of energy deposition, then the value of $f_m^i(E_m)$ is the conditional probability, or likelihood, that this module's response was induced by particle type i. Here the word conditional is used to emphasize that this quantity is not the probability that the track *was* particle type i, but the probability of obtaining this response *if* the incident particle was type i.

If the results from all TRD modules can be assumed to be nearly independent then they can be combined as independent probabilities according to

$$P_{TRD}^{c,i}(\bar{E}) = \prod_{m=1}^{6} f_m^i(E_m). \tag{6.2}$$

Here $P_{TRD}^{c,i}(\bar{E})$ is the conditional probability that particle type i would have induced the combined TRD response $\bar{E}$. The fact the $P_{TRD}^{c,i}$ will in general be small should not be alarming, noting that it is the relative magnitude of the $P_{TRD}^{c,i}$ for each particle type i which will be the source of identifying the particle type of maximum likelihood.

Assuming the independence of results from the various PID detectors, namely the Cerenkov, TRD, preshower, and calorimeter, these detector probabilities can be combined by the same multiplication method:

$$P^{c,i} = \prod_{d=1}^{4} P_d^{c,i}. \tag{6.3}$$

Here the subscript d denotes each PID detector. The track now can be associated with the particle type i which has maximum likelihood, that is, greatest relative magnitude of $P^{c,i}$. The above method however fails to provide any quantitative measure of the relative contamination from other particle types since it doesn't make use of the actual incident flux information. This effect was shown to be crucial in section 6.1.

A quantitative measure of this contamination can be obtained from knowledge of the *a posteriori* probability that the track in question can be correctly identified with particle type i . The relationship between this last probability and the conditional one given in eq. 6.3 is defined by Bayes Theorem [32],

$$P(C_i|E_j) = \frac{P(E_j|C_i)P(C_i)}{\sum_i P(E_j|C_i)P(C_i)}, \tag{6.4}$$

which reads: the probability that effect E_j can be attributed to cause C_i is proportional to the probability that cause C_i would lead to effect E_j times the probability of occurrence of cause C_i [32].

The factors $P(C_i)$ in the case of HERMES PID are the relative incident rates for each particle type. Thus the factors $P(C_i)$ are the necessary weighting factors of the distributions $f^i(E)$ motivated earlier.

Although the ratio of background hadrons to positrons is known to be a strong function of momentum and scattering angle, the exact dependence is not known. This leads to the observation that the usefulness of Bayes Theorem seems limited since *a priori* knowledge of these relative flux rates are required. This limitation may be overcome, however, by an iterative procedure which fits the observed event rates to the known distributions. This procedure allows for determination of the flux ratio of pions to positrons, or, equivalently, for determination of the flux factors $P(C_i)$. The algorithm for this iterative procedure will be presented at the end of the following section.

6.3 Particle Identification Algorithms

In light of the above considerations it is now possible to introduce the PID algorithms. These algorithms apply the above formulae to the interpretation of the detector responses as quantitative probabilities that a given track can be identified with each particle candidate i.

6.3.1 TRD PID Algorithm

The generated $f^i(E)$ distributions of section 5.5.4 were stored in arrays for use in the HERMES reconstruction (HRC) program. This program uses the position information from the tracking chambers to reconstruct particle tracks in the front and back regions of the spectrometer. The front and back segments are then combined, if possible, according to deflection through the magnetic field. The magnitude of this deflection determines the momentum of the particle.

The TRD PID algorithm uses the back segment of the track to determine which TRD wire cells were struck, and, if the track crossed two wire cells in a given module (which determination is also constrained by the alignment resolution) then the energy deposition values from these wire cells are summed. In either case, for each module the energy deposition value E_m is obtained after gain calibrations are applied. The values of $f_m^i(E_m)$ are then extracted from the generated distributions for each module m and particle type i.

Recalling that there are 9 such $f_m^i(E_m)$ values reflecting permutations of incident angle and momentum, these 9 values for each i and m are then interpolated to the value of incident angle and momentum determined from the track reconstruction. This double interpolation results in the set of numbers $f_m^i(E_m)$. The results for the six modules are then combined using eq. 6.2 to obtain $P_{TRD}^{c,i}(\bar{E})$ for each particle type i. This last step approximates that the responses from separate modules are independent measurements. Correlation effects can be included if the multiplication in eq. 6.2 is replaced with a 6 dimensional matrix containing the distribution of combined six module responses, $\bar{E}$, for each particle type. Such an approach would require a large investment of CPU time if performed with simulation. In light of the inexact nature of simulation data and the significant investment of CPU time, such a study of the second order biases which result from neglecting correlations is best reserved for once data are available to determine the accuracy of simulation results.

6.3.2 Proposed HERMES PID Algorithm

The remaining task is to combine the results of all detectors according to eq. 6.3, yielding values of $P^{c,i}(\bar{E})$ for each track. Correlations may be included in a manner analogous to that for combining the TRD conditional probabilities, but again such a study is best deferred until experimental data are available.

The conditional probabilities for each particle type can be converted to final *a posteriori* probabilities through application of Bayes Theorem:

$$P^i(\bar{E}) = \frac{P^{c,i}(\bar{E})P^i_F(p,\theta)}{\sum_i P^{c,i}(\bar{E})P^i_F(p,\theta)}, \tag{6.5}$$

where $P^i(\bar{E})$ is the final probability that the combined detector responses $\bar{E}$ for the track in question can be identified with particle type i, and where $P^i_F(p,\theta)$ and $P^{c,i}(\bar{E})$ are the flux factor and combined detector conditional probability corresponding to the given incident track angle and momentum. Precise knowledge of the flux factors allows for maximum positron efficiency as a function of incident angle and momentum for a given hadron contamination threshold.

The factors $P^i_F(p,\theta)$ can be obtained from a Bayesian iteration procedure following that of ref. [32]. Given a set of initial guesses for the relative flux rates, $P^{i,\prime}_F(p,\theta)$, a first application of Bayes theorem allows for assignment of the expected number of events to each particle type i according to:

$$n'(i) = \sum_j n_{obs}(\bar{E}_j) \cdot P^{c,i}(\bar{E}_j), \tag{6.6}$$

where n_{obs} is the total number of events at a given incident angle and momentum and for a given permutation $\bar{E}_j$ of detector responses.

The initial guesses for the relative flux rates can then be improved with the estimate:

$$P^{i,\prime\prime}_F(p,\theta) = \frac{n'(i)}{N_{obs}(p,\theta)}, \tag{6.7}$$

where,

$$N_{obs} = \sum_j n_{obs}(\bar{E}_j). \tag{6.8}$$

This procedure is repeated iteratively until convergence within an acceptable χ^2 between the last two flux estimates is achieved.

The optimal flux factor binning in incident angle and momentum which is necessary for the implementation of this procedure depends on the amount and distribution of experimental data, as well as the precision required of the probability analysis. Further, the Bayes iteration algorithm is sufficiently flexible to accommodate correlation effects between detectors. This corresponds to the case when the conditional probability matrix, $P^{c,i}(\bar{E}_j)$, is constructed explicitly rather than obtained from a multiplication of individual detector probabilities. In fact, since the combined responses $n_{obs}(\bar{E}_j)$ automatically include correlations, the flux factors obtained from the Bayes iteration should be more accurate when the conditional probability matrix includes these correlation effects.

Chapter 7

Conclusion

The HERMES experiment is currently being commissioned and data collection will begin shortly. The experiment anticipates to contribute important knowledge to our understanding of the origin of the nucleon spin.

The TRD plays an essential role in the particle identification system of the HERMES spectrometer. Prototype tests of the TRD were performed studying various radiator types and the 17–20 micron fibre radiators proved, to first order, to be capable of providing sufficient particle separation for the HERMES TRD to reach its design pion rejection factor goal. The test data also served as an important standard for the optimisation of Monte Carlo simulation of the six module HERMES TRD.

Monte Carlo modeling is necessary not only for optimisation of the HERMES TRD design, but also for studies of the TRD performance and interpretation of the TRD data. Since the Monte Carlo of the complete HERMES experiment (HMC) was based on the GEANT detector simulation tool and since the TRD performance is uniquely sensitive to low energy physics processes, an independent simulation of the prototype TRD was developed using the GEANT tools in order to test and optimise their accuracy. Different models of energy loss and the important impact of low energy δ-ray tracking were studied. An algorithm for the generation of transition radiation (TR) in the irregular fibre radiator was also obtained from an earlier simulation and integrated with the GEANT physics modeling algorithms.

The optimised results of the TRD simulation were found to be in good agreement

with the available prototype TRD data. Following this success, the prototype TRD algorithms were integrated into the HMC simulation. The prototype TRD simulation was then also modified and extended into an independent simulation of the six module HERMES TRD, including some significant effects from the HERMES spectrometer environment. This simulation was then available for fast and flexible studies of the TRD performance.

The first application of this independent TRD simulation was in studies for optimising the particle identification (PID) algorithms required for interpretation of the TRD response. In particular, the sources of variation in the TRD response distributions needed to be identified and determined. Further, a set of response distributions spanning the range of these variations had to be generated for use in the PID algorithms.

These Monte Carlo studies confirmed the anticipated kinematic variations but also revealed important unanticipated detector dependent effects in the response distributions. In particular, the cumulative effect of 'punch-through' TR was found to be significant, ultimately enhancing the particle separation of downstream modules. In light of these studies a set of distributions were generated for use in the PID algorithms.

Once the nature and magnitude of the variation of the energy deposition distributions had been determined, TRD particle identification algorithms were developed which apply these distributions to the interpretation of TRD results. Further, a PID algorithm for combining the results of all HERMES PID detectors was also developed which accommodates the relative flux factors necessary for quantitative measure of the actual hadron contamination of the positron data sample. Finally, an iterative algorithm is proposed which measures the precise incident angle and momentum dependence of the relative flux factor rates for each particle type for use in the HERMES PID probability algorithm.

Appendix: Contribution to HERMES

Modern high energy experiments have come to require the combined effort of many physicists, students, and technicians to efficiently achieve the desired physics goals. In light of this group effort, the contribution of any one individual can be difficult to identify. Thus, at the request of my supervisory committee, this appendix is provided to specify my primary contributions to the HERMES experiment.

My involvement with HERMES began in September 1993 and my primary task until October 1994 was the construction of the TRD at TRIUMF. This involvement was in parallel with course work and extends over the complete construction phase of the TRD.

During the summer of 1994 I began to acquire familiarity with the HERMES software. At that time the task of developing and testing algorithms for the modeling of the TRD which could be integrated with the existing HERMES software was presented to me. This involved software work at TRIUMF and also two short trips to DESY for software workshops.

Through the remainder of the fall of 1994 my primary responsibility became software development and analysis of the existing prototype TRD data which had been taken prior to my involvement with HERMES. After the completion of my course work requirements at the end of the fall term of 1994 I began to work full time at DESY. In parallel with continued software development I contributed about one third of my time to the final phase of the installation of the TRD.

In the spring of 1995 I completed the Monte Carlo studies of the TRD response

distributions and developed the PID algorithms for the TRD and for the general HERMES PID analysis. This work was supplemented with contributions to the instrumentation of the high voltage and electronics readout of the TRD, as well as with involvement in preliminary commissioning of the TRD. In the late spring and early summer of 1995 I also ran data taking shifts during commissioning runs for the HERMES spectrometer.

Bibliography

[1] EMC Collaboration, J. Ashman *et al.*, Phys. Lett. B 206, 1 (1988).

[2] F.E. Close, The Nucleon Spin Crisis Bible, RAL-93-034 (1993).

[3] F. Halzen and A. Martin, Quarks and Leptons, John Wiley & Sons, Inc. (1984).

[4] E. Hughes, Polarized Lepton-Nucleon Scattering, SLAC-PUB-6439 (1994).

[5] M. Vetterli, Deep Inelastic Lepton Scattering Lecture Notes, TRIUMF Summer Institute (1993), unpublished.

[6] HERMES Collaboration, *Technical Design Report*, DESY-PRC 93/06 (1993).

[7] F.E. Close and R.G. Roberts, Consistent Analysis of the Spin Content of the Nucleon, RAL-93-040 (1993).

[8] G.G., Ross and R.G. Roberts, The Gluon Contribution to Polarised Nucleon Structure Functions, RAL-90-062 (1990).

[9] EMC Collaboration, J. Ashman *et al.*, Nucl. Phys. B 328, 1 (1989).

[10] SMC Collaboration, B. Adeva *et al.*, Phys. Lett. B 302, 533 (1993).

[11] SMC Collaboration, D. Adam *et al.*, Phys. Lett. B 329, 399 (1994).

[12] E142 Collaboration, P.L. Anthony *et al.*, Phys. Rev. Lett. 71, 959 (1993).

[13] E143 Collaboration, K. Abe *et al.*, Phys. Rev. Lett. 74 346 (1995).

[14] E143 Collaboration, K. Abe *et al.*, Phys. Rev. Lett. 75, 25 (1995).

[15] M. Dueren and K. Zapfe, Experimental Techniques and Physics in a Polarised Storage Ring, DESY 94-238 (1994).

[16] E. Berger, Semi-Inclusive Inelastic Scattering From Nuclei, ANL-HEP-PR-87-45 (1987).

[17] R. Feynman, Photon-Hadron Interactions, W.A. Benjamin, Inc. (1972).

[18] B.D. Burow *et al.*, Photoproduction Physics at HERA, DESY 94-215 (1994).

[19] R.Fernow, Introduction to Experimental Particle Physics, Cambridge University Press (1986).

[20] V.L. Ginzburg and I.M. Frank, Zh.Eksp. Teor. Fiz. 16, 15 (1946).

[21] G.M. Garibian, Zh. Eksp. Teor. Fiz. 33, 1043 (1957).

[22] G.M. Garibian, Zh. Eksp. Teor. Fiz. 37, 527 (1959).

[23] X. Artru, G.B. Yodh, and G. Mennessier, Physical Review D 12, 1289 (1975).

[24] B. Dolgoshein, Nuclear Instruments and Methods in Physics Research A326, 434 (1993).

[25] F. Sauli, Principles of Operation of Multiwire Proportional and Drift Chambers, CERN 77-09 (1977).

[26] GEANT Detector Description and Simulation Tool, CERN Program Library Long Writeup, W5013 (1994).

[27] V.C. Ermilova, L.P. Kotenko, and G.I. Merzon, Nuclear Intruments and Methods 145, 555 (1977).

[28] S. Ravndall, private communication.

[29] A. Miller, private communication.

[30] G.M. Garibian, L.A. Gevorgian, and C.Yang, Nuclear Instruments and Methods 125, 133 (1975).

[31] S. Brandt, Statistical and Computational Methods in Data Analysis, North-Holland Publishing Company (1976).

[32] G. D'Agostini, A Multidimensional Unfolding Method Based on Bayes' Theorem, DESY 94-099 (1994).